# DVB-T based Passive Forward Scatter Radar: inherent limitations and enabling solutions

Fabiola Colone
DIET Dept. Sapienza, University of Rome
Via Eudossiana 18, 00184 - Rome, Italy
fabiola.colone@uniroma1.it

***Abstract*—This paper investigates the target detection capability of a Passive Forward Scatter Radar (PFSR) exploiting a Digital Video Broadcasting – Terrestrial (DVB-T) transmitter as illuminator of opportunity. By means of theoretical and simulated analyses, it is shown that conventional processing schemes might suffer from a significant performance degradation when exploiting Orthogonal Frequency Division Multiplexing (OFDM) waveforms of opportunity compared to other broadcast transmissions (e.g. Frequency Modulation radio broadcast). Specifically, the direct application of conventional processing approaches to the case of a DVB-T PFSR is demonstrated to yield (i) a non-negligible increase of the competing background level and (ii) a steeper fading of the target response due to the intrinsic characteristics of the exploited waveforms of opportunity, above all the modulation scheme and the signal spectral characteristics.**

**Therefore, appropriate signal processing techniques are proposed to avoid these effects which jeopardize the target detection capability. The conceived processing scheme exploits the digital nature of the employed waveforms and a sub-band approach for improving both the interference cancellation stage and the target signature extraction. The benefits of the proposed approach are illustrated by means of theoretical and simulated analyses. The application of the resulting processing scheme against experimental data proves its effectiveness in practical scenarios.**

***Keywords*—Passive Forward Scatter Radar; DVB-T; OFDM; target detection; cancellation.***

## I. INTRODUCTION

Over the past two decades, passive radar (PR) has received a considerable attention with an astonishing number of contributions being appeared in the technical literature, see e.g. [1]-[6] and the references therein. The advantages and drawbacks of such systems are well known and inherently caused by the exploitation of pre-existent radio frequency transmitters as illuminators of opportunity (IOs) to detect and track targets. The wide interest received by PR sensors allowed them to increasingly reach a point of maturity in a number of surveillance applications at both long range and short range. Nevertheless, the effectiveness of such sensors has been usually investigated under conventional acquisition geometries. Specifically, quasi-monostatic and moderate bistatic configurations have been exploited in most of the reported theoretical studies and experimental demonstrations.

Recently, after the renewed interest obtained in active radar applications [7][8], different studies appeared in the technical literature addressing the exploitation of extreme bistatic configurations, namely the Forward Scatter (FS) configuration, in passive radars [9]-[22].

This configuration occurs when the angle subtended between transmitter (Tx), target and receiver (Rx), namely the bistatic angle, is close to 180° so that the target is observed as it crosses the Tx-Rx baseline. In such geometry, the "forward scattering" mechanism is invoked to model the energy scattered by the target that results in a shadowing effect on the direct signal received from the Tx [7][8][24]. If properly exploited, this effect yields in a number of advantages compared to traditional monostatic or moderate bistatic geometries, such as enhanced target radar cross-section (RCS), robustness to stealth technology, and limited hardware complexity [7][8],[23]-[25].

The studies reported in the open literature addressing passive forward scatter radar (PFSR) have investigated the above aspects when parasitically exploiting different illuminators of opportunity operating from Very High Frequency (VHF) to K bands [11], there including Global Navigation Satellite System (GNSS) transmitters [9][10][13][17][18], Global System for Mobile Communications (GSM) and Long-Term Evolution (LTE) base stations [12][20], radio and television broadcast transmitters [14][15][22], and WiFi access points [16][19][21]. Many of these studies focused on the capability of a PFSR to detect and track ground-based or aerial targets, whereas some of them have investigated the potential for improved automatic target classification [18]-[21].

The possibility to exploit existing transmitters further reduces the system complexity, as it only requires the design and implementation of the passive receiver, while enhancing its pervasiveness thanks to the availability of a dense network of transmitters. This is certainly the case for broadcast radio and television transmitters. The effectiveness of a PFSR based on terrestrial transmitters operating in the VHF and Ultra High Frequency (UHF) bands has been demonstrated in [14] for aircrafts detection. The authors of [14] proved that a simple Rx experimental setup and a straightforward processing scheme can be adopted to effectively detect targets as they move along their path. Thanks to the high number of Frequency Modulation (FM) radio broadcasting, Digital Audio Broadcasting (DAB), or Digital Video Broadcasting – Terrestrial (DVB-T) emitters potentially available in a given region, the study in [14] paves the way to innovative low-cost solutions for airspace surveillance, particularly suited for low-flying aircrafts.

In this paper, we aim at further improving the results in [14] for the case of a DVB-T based PFSR. In fact, we first observe that the signal processing chain employed in [14] is waveform-

independent and we show that the direct application to a PFSR exploiting Orthogonal Frequency Division Multiplexing (OFDM) transmissions does not provide robust performance. To this purpose, we extend the preliminary investigations in [22] and we compare the results for DVB-T based PFSR and FM-based PFSR, by means of theoretical and simulated analyses. The results prove that a significant performance degradation is experienced in the DVB-T case, due to the intrinsic characteristics of the employed digital waveforms. Specifically, it is shown that the competing background against which the target signature is detected in the time-frequency domain might be significantly higher when exploiting OFDM signals in lieu of FM signals. Moreover, the spectral characteristics of the DVB-T signals might be responsible of a faster decay of the target signature as the target moves away from the baseline. Whilst the limitations above are investigated for the case of DVB-T signals, the underlying motivations might be common to several waveforms of opportunity exploited in PFSR applications.

Therefore, we propose appropriate modifications to the processing scheme in [14] aiming at mitigating the observed effects while keeping low its complexity. By exploiting the digital nature of the considered waveforms of opportunity, the proposed approach is based on the removal of the fast-varying amplitude modulation effect induced on the received signal by the employed OFDM signal. Moreover, a sub-band approach is proposed to mitigate the decay of the target signature due to the autocorrelation properties of the considered signals of opportunity. Theoretical and simulated analyses prove the benefits of the proposed scheme which is shown to allow improved detection capability against typical targets of interest. Also a practical demonstration of its effectiveness is reported against experimental data collected by a commercial off-the-shelf (COTS) based receiver fielded at Sapienza University of Rome.

The paper is organized as follows. The adopted signal model is described in Section II together with the conventional processing scheme adopted in FSR. In Section III the limitations of this approach are illustrated for the case of a PFSR exploiting DVB-T signals. The identified limitations are then separately addressed in the subsequent two sections where the proposed solutions are presented. Section VI reports the comparative analysis of the new processing scheme with conventional approaches in terms of both theoretical and simulated performance as well as by means of application to experimental data. Finally, concluding remarks are given in Section VI while mathematical details are reported in the Appendices.

## II. Passive Forward-Scatter Signal Model and Processing Scheme

The adopted signal model and the basic signal processing scheme for PFSR are summarized in the following sub-sections.

### A. Signal model

The considered geometry is sketched in Fig. 1.

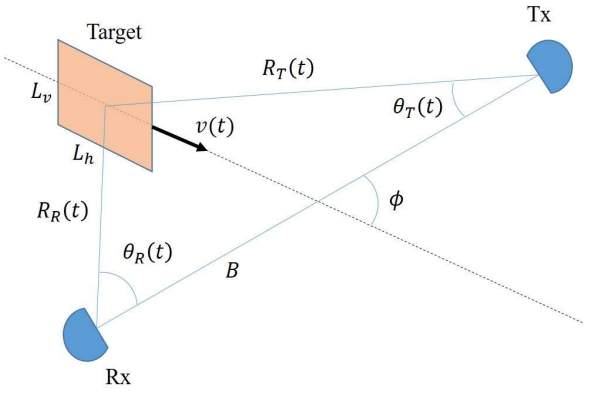


Fig. 1. Forward scatter radar geometry.

The Tx-Rx baseline has length $B$. The target is assumed to be of a rectangular shape with horizontal dimensions $L_h$ and vertical dimension $L_v$, being $L_v, L_h \gg \lambda$ where $\lambda$ is the wavelength associated to the carrier frequency of the employed signal of opportunity. The target moves with instantaneous velocity $v(t)$ along a rectilinear trajectory that crosses the baseline with an incidence angle $\phi$.

The time-varying distance of the target from the Tx and the Rx are described by $R_T(t)$ and $R_R(t)$, respectively, and we assume that the target lies on the Tx-Rx baseline at $t$=0. Correspondingly, $\theta_T(t)$ and $\theta_R(t)$ encode the instantaneous angle between the baseline and the target line-of-sight (LOS) at the Tx and Rx, respectively.

As the target moves along its path, the equivalent baseband signal collected by the Rx antenna is written as the sum of three main contributions:

$$x(t) = A_D s(t) + A_T(t) e^{j\varphi(t)} s\big(t - \tau(t)\big) + n(t) \qquad (1)$$

The first term on the right hand side (r.h.s.) of (1) represents the direct signal from the Tx and it is obtained as the product of a constant complex amplitude, $A_D$, encoding the Tx-to-Rx propagation, and the equivalent baseband signal, s$(t)$, emitted by the Tx of opportunity with bandwidth $B_s$. We assume this signal to be a unitary power continuous transmission whose characteristics depend on the modulation scheme adopted by the corresponding broadcast service standard. For instance, it corresponds to an analog frequency modulated signal when FM radio broadcast transmissions are exploited. In contrast, DAB and DVB-T emitters use OFDM modulation schemes to broadcast radio and television programs.

The second term on the r.h.s. of (1) represents the target signal contribution. For narrowband waveforms of opportunity, it is given by the product of three factors listed below.

- The complex amplitude $A_T(t)$ encapsulates the Tx-target-Rx path loss, as well as the target dimensions perceived by the system according to the instantaneous geometry. Assuming that the target remains in the far field condition from both Tx and Rx, its amplitude can be approximated using the model in [25]:

$$A_T(t) = j\frac{L_v L_h B}{\lambda R_T(t) R_R(t)} A_D \times \frac{1}{2}\{cos[\theta_T(t) - \phi] + cos[\theta_R(t) + \phi]\} \times sinc\left\{\frac{L_h}{\lambda}[sin(\theta_T(t) - \phi) + sin(\theta_R(t) + \phi)]\right\} \quad (2)$$

- The exponential term $e^{j\varphi(t)}$ encodes the instantaneous phase shift of the target signal with respect to the direct signal, being

$$\varphi(t) = \frac{2\pi}{\lambda}[R_T(t) + R_R(t) - B] \quad (3)$$

- The time-shifted copy of the transmitted signal, $s\big(t - \tau(t)\big)$, where the delay is evaluated relative to the direct signal:

$$\tau(t) = \frac{R_T(t) + R_R(t) - B}{c} \quad (4)$$

The numerator of (4) defines the relative bistatic range, namely the difference between the two-way Tx-target-Rx distance, $R_T(t) + R_R(t)$, and the baseline $B$.

Finally, the last term on the r.h.s. of (1) represents the noise at the Rx that is modeled as an additive white Gaussian noise (AWGN) with variance $\sigma_N^2$, statistically independent of the first two signal components. According to the positions above, the direct-signal-to-noise power ratio (DNR) is defined as:

$$\mathrm{DNR} = \frac{P_D}{\sigma_N^2} = \frac{|A_D|^2}{\sigma_N^2} \quad (5)$$

### *B. Processing scheme*

The detection of a target is sought by analyzing the amplitude modulation produced on the direct signal as it crosses the Tx-Rx baseline. Such effect is a combination of the target signal instantaneous phase (see eq. (3)) and its scattering pattern (see eq. (2)) and it is expected to be quite stable in a small angular region encompassing the first sidelobes of the target's response in (2). Therefore, assuming that a sufficient DNR is available at the Rx site, a simple signal processing scheme might be employed to extract the target's signature from the received signals [14]. The main blocks of this basic signal processing scheme are sketched in Fig. 2 and they basically resemble the conventional approaches adopted in active FSR employing pure tone sinusoidal waveforms [7][8][25].

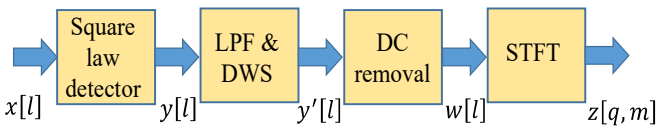


Fig. 2. Conventional FSR signal processing scheme.

It is assumed that the input to this scheme is the properly sampled version of the signal in (1):

$$x[l] = A_D s[l] + A_T[l] e^{j\varphi[l]} s^{(\tau[l])}[l] + n[l] \quad (l \in \mathbb{Z}) \quad (6)$$

where $s^{(\tau[l])}[l]$ indicates the $l$-th sample of the time-shifted version of $s(t)$, delayed by a delay equal to $\tau[l]$, i.e. $s^{(\tau[l])}[l] = s\left(\frac{l}{f_s} - \tau[l]\right)$, $f_s$ being the sampling frequency.

After the extraction of the square modulus, the obtained signal $y[l] = |x[l]|^2$ is filtered using a low-pass filter (LPF) with bandwidth $B_{LPF}$, which is designed to remove frequency components outside the range of the expected target Doppler frequencies.

As stated in [14], as for any Doppler radar, the LPF design depends on the scenario of interest. The LPF also features a downsampling stage (DWS), which reduces signal sample rate to $f_s'$ by taking into account its output bandwidth.Consequently, the downsampling factor is defined as $\eta_{LPF} = f_s'/f_s$, which encodes the resulting narrowing of the bandwidth if the sampling frequency is selected according to a Nyquist criterion, i.e. $B_{LPF} = \eta_{LPF} B_s$.

The output signal $y'[l]$ will be then passed through a DC component removal stage. The output of this stage is

$$w[l] = y'[l] - \overline{y'[l]} \quad (7)$$

where $\overline{y'[l]}$ represents the average value of the signal $y'[l]$ evaluated over an appropriate temporal interval $T_{DC}$. The resulting signal then undergoes a Short-Time Fourier Transform (STFT), which provides its time-frequency analysis. Specifically, the STFT is computed by taking the fast Fourier transform (FFT) of short consecutive signal fragments of $L$ samples each. At the $q$-th fragment we obtain:

$$z[q,m] = \sum_{l=0}^{L-1} h[l] w[l_0 + q(L - L_{ovl}) + l] e^{-j2\pi ml/L} \quad (8)$$

where $w[l_0]$ represents the first processed sample of the considered acquisition, an overlap of $L_{ovl}$ samples is considered among consecutively processed signal fragments, $h[l]$ is the $l$-th coefficient of an appropriate real-valued weighting function employed to limit the sidelobes level of the Doppler response, the indices $q$ and $m$ span the time and Doppler axes, respectively. Please note that, if the length $L$ of the considered fragment is kept small, eq. (8) approximates a matched filter for any target contribution that appears as constant in amplitude and linearly varying in phase over short Coherent Processing Intervals (CPI). Alternative solutions could be exploited at this stage by resorting to a matched filter that operates over longer integration times and compensates for the time-varying (chirped) Doppler variation [25][26]. However such approach requires an increase computational complexity since a bank of matched filters is typically required for an effective operation. Therefore, in this paper, following the approach of [14], we

adopt the STFT as a simple and effective solution.

By collecting the intensity of the output of eq. (8) at consecutive fragments for positive frequency values (the results are symmetrical about zero), a spectrogram is obtained where the typical V-shaped target signature can be easily recognized, which indicates the absolute value of the target bistatic velocity across time [14].

## III. LIMITATIONS FOR A DVB-T BASED PFSR

In this section, the limitations of the processing scheme summarized in sub-section II.B are analyzed when DVB-T transmissions are employed as waveforms of opportunity. Firstly, some simulated results are reported in Section III.A, where these limitations are clearly identified and compared to the case of FM radio signals. Then, in the subsequent sub-sections III.B and III.C, a theoretical analysis is performed to provide a deeper insight into the cause and the extent of the identified shortcomings.

### *A. Example of results against simulated case studies*

In order to investigate the robustness of the processing scheme summarized in sub-section II.B when different waveforms of opportunity are employed, a signal simulator was built according to the signal model described in sub-section II.A. It accepts as inputs the signals generated according to different transmission standards (e.g. FM radio, DVB-T, etc.) and exploits a stop-and-go strategy over extremely short signal fragments to simulate the continuous motion of the target as it crosses the baseline.

In the following, the results are shown for the case study whose main parameters are reported in Table I. A rectangular shaped target is considered with dimensions resembling those of a small airplane. It moves at constant velocity and crosses the baseline at its middle point with $\phi$=90° incident angle.

TABLE I
SIMULATED CASE STUDY PARAMETERS

| Description | Symbol | Value | |
|---|---|---|---|
| Tx-Rx Baseline | $B$ | 40 km | |
| Target hor. dim. | $L_h$ | 15 m | |
| Target vert. dim | $L_v$ | 3 m | |
| Target speed | v | 75 m/s | |
| Crossing point | $R_R(0)$ | 20 km | |
| Incidence angle | $\phi$ | 90 deg | |
| Direct signal to noise Ratio | DNR | [20 – 40] dB | |
| Observation interval | | 80 s | |
| | | FM radio | DVB-T |
| Carrier frequency | $f_c$ | 100 MHz | 600 MHz |
| Wavelength | $\lambda$ | 3 m | 0.5 m |
| Signal bandwidth | $B_s$ | 200 kHz | 7.62 MHz |
| Sampling frequency | $f_s$ | 200 kHz | 64/7 MHz |

The same case study is simulated for a PFSR exploiting FM radio or DVB-T transmissions, by properly modifying the parameters related to the corresponding broadcast standard, i.e. carrier frequency, modulation scheme and resulting bandwidth, and sampling frequency.

The simulated signals are then processed according to the scheme described in sub-section II.B with parameters reported in Table II. Whilst the exploitation of different waveforms of opportunity might set different constraints on the parameters selected for each signal processing stage, in the following we adopt the same set of parameters for both the FM radio based PFSR and the DVB-T based PFSR in order to better illustrate their differences.

TABLE II
SIGNAL PROCESSING PARAMETERS

| Description | Symbol | Value |
|---|---|---|
| Coherent Processing Interval | $CPI$ | 1 s |
| Fragments overlap | $T_{ovl}$ | 0.9 s |
| Interval for DC est. | $T_{DC}$ | 1 s |
| Weighting Function | $h[l]$ | Hamming |
| LPF cut-off freq. | $f_{LPF}$ | 100 Hz |
| Sampling frequency after dec. | $f_s'$ | 223 Hz |

Specifically, the same CPI length is used, which is set in order to avoid significant Doppler migration in the DVB-T case. In addition, the same cut-off frequency $f_{LPF}$=100 Hz is used for the LPF, namely $B_{LPF}$=200 Hz. This selection allows to preserve target returns at bistatic velocities (sum of relative velocities with respect to the Tx and the Rx) up to 50 m/s in the DVB-T case and up to 300 m/s in the FM case. Please notice that, in the considered case study, the highest observed value for the target bistatic velocity is about 25 m/s and this value is well below the maximum observable value in both systems considered.

The output of the LPF after decimation is reported in Fig. 3(a-b) for the considered case study when a FM radio signal or a DVB-T signal are used as waveforms of opportunity, respectively.

In this example, the DNR is set to 40 dB. Correspondingly, the spectrograms obtained at the output of the Doppler processing stage are reported in Fig. 3(c-d). For a direct comparison, the two spectrograms have been scaled to a reference noise power level as expected at the output of the processing scheme (see details in the following sub-section). In addition, the Doppler frequencies have been mapped into a common bistatic velocity axis, $v_b = \lambda f_D$.

In all figures, the target signature is apparent. As expected from (2), the peak value measured in the DVB-T based PFSR spectrogram is higher than that for the FM spectrogram due to the higher carrier frequency. For the same reason, the FM spectrogram has a degraded velocity resolution but it shows a target response that exists at a level significantly higher than the background for a longer time. In contrast, the target signature observed in the DVB-T spectrogram rapidly decays and

This article has been accepted for publication in a future issue of this journal, but has not been fully edited. Content may change prior to final publication. Citation information: DOI 10.1109/TAES.2020.3035435, IEEE Transactions on Aerospace and Electronic Systems



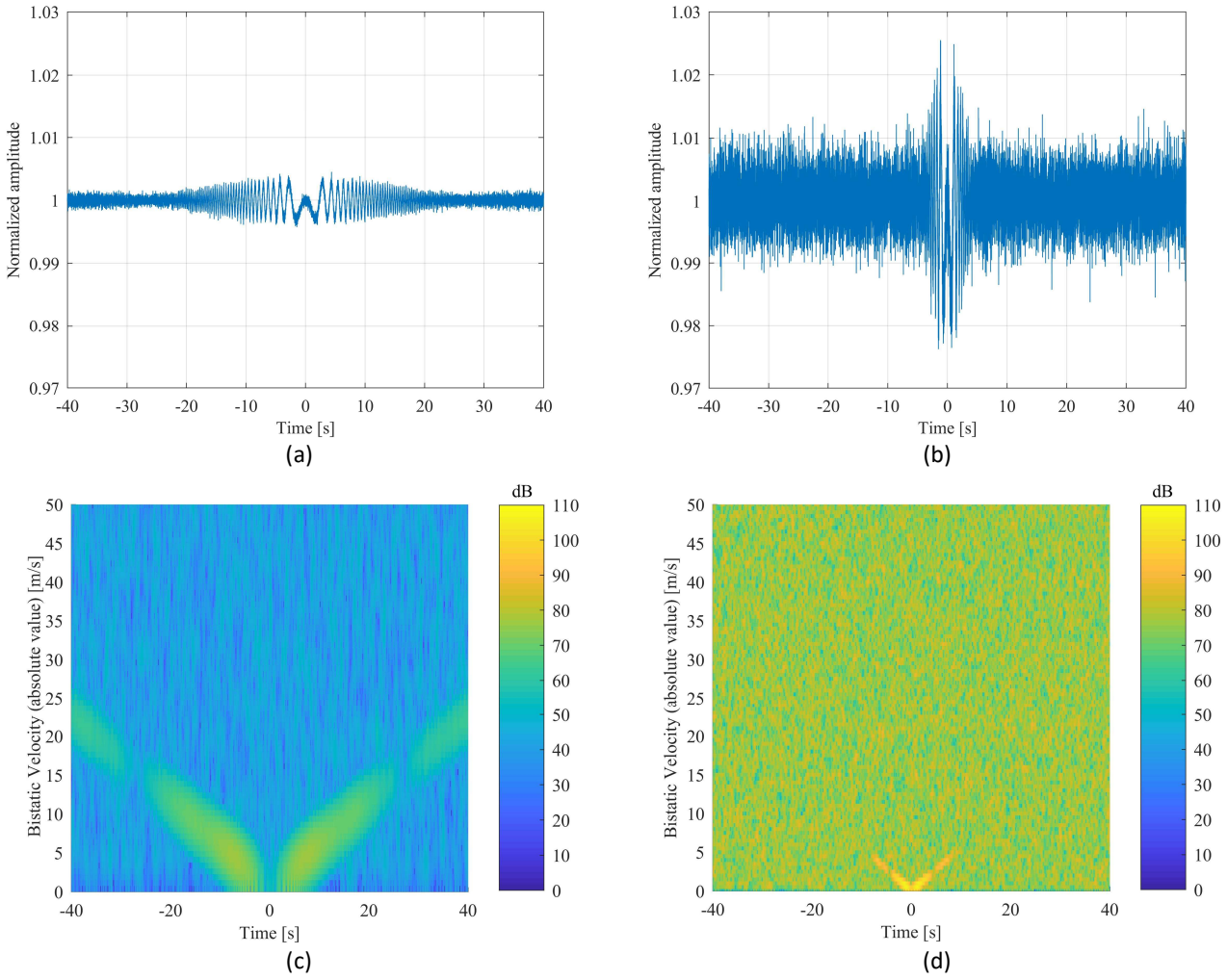


Fig. 3. Results of the conventional PFSR processing scheme for the considered case-study (DNR=40 dB): output of the LPF for FM based PFSR (a) and DVB-T based PFSR (b); spectrograms obtained for FM based PFSR (c) and DVB-T based PFSR (d).

eventually it is masked by a severe background, which appears to be much higher than that observed in the FM spectrogram.

In the following, we demonstrate that these effects do not depend solely on the shorter wavelength associated with DVB-T signals but rather they are caused by intrinsic characteristics of the employed DVB-T waveforms. Understanding the causes and the extent of these effects is essential to devise enabling solutions for effective DVB-T based PFSR.

### *B. Background Level Increase*

Aiming at predicting the background level in the final PFSR spectrogram, in this section we characterize the power level of the FFT block output $z[q,m]$ in Fig. 2 in the absence of target, i.e. under hypothesis $H_0$.

In Appendix A, it is shown that the statistical mean value of the output, namely $E\{z[q,m]|H_0\}$, is zero independently of the employed waveform provided that the average value of the signal $y'[l]$ in (7) is an unbiased estimator of its statistical mean value, i.e. $E\{\overline{y'[l]}\} = E\{y'[l]\}$.

In contrast, the second moment, namely the output disturbance power level in the final spectrogram, depends on the employed waveform of opportunity.

For both the case of FM and DVB-T transmissions, we model the corresponding signal as a wide sense stationary stochastic complex process, spectrally white in the Rx bandwidth.

However, when a FM radio transmission is used, the signal exhibits a constant amplitude $A_s$ while the instantaneous random phase is assumed to be uniformly distributed in $[0,2\pi]$.

Under such hypothesis, the second moment of the generic pixel in the output spectrogram is given by (see Appendix A, eq.(41)):

$$E\{|z[q,m]|^2|H_0, FM\ case\} = \left\{\sum_{l=0}^{L-1} h^2[l]\right\}\eta_{LPF}\sigma_N^4\,(1+2\,DNR) \quad (9)$$

The factor $F = \{\sum_{l=0}^{L-1} h^2[l]\}\eta_{LPF}\sigma_N^4$ represents the output power level that would have appeared in the absence of the direct signal, namely that solely due to the noise at the Rx. That factor depends on the adopted weighting function, the LPF selectivity and the Rx noise level and it has been used in Fig. 3(c) to scale the spectrogram obtained for the FM case study. As a consequence, the observed background level appears at $[1 + 2\,DNR] \cong 43\,dB$ above the reference 0 dB level, as correctly predicted by (9).

When a DVB-T transmitter is employed as illuminator of opportunity, the corresponding waveform is an OFDM signal where different sub-carriers are assumed to be modulated by statistically independent streams of equiprobable symbols based on a quadrature amplitude modulation (QAM) scheme, which employs a constellation of dimension $M_C$. According to the DVB-T standard, possible modulation schemes are QPSK ($M_C = 4$), 16-QAM ($M_C = 16$), and 64-QAM ($M_C = 64$) and we define the corresponding constellation so that it shows an average power independent of the adopted scheme, i.e. $C = \frac{1}{M_C}\sum_{p=0}^{M_C-1}|c_p|^2$, being $\{c_p\}_{p=0,..,M_C-1}$ the constellation symbols of the corresponding constellation map. Under such hypotheses, the second moment of the generic pixel in the output spectrogram is given by (see Appendix A, eq. (44)):

$$E\{|z[q,m]|^2|H_0, DVB-T\ case\} = \left\{\sum_{l=0}^{L-1} h^2[l]\right\}\eta_{LPF}\sigma_N^4\left[(1+DNR)^2 + DNR^2\left(\frac{\mu-2}{N_c}\right)\right] \quad (10)$$

where $\mu = \frac{1}{M_C}\sum_{p=0}^{M_C-1}\frac{|c_p|^4}{C^2}$ is dependent on the adopted modulation scheme. In detail, we have $\mu = 1$ for $M_C = 4$, $\mu = 1.32$ for $M_C = 16$, and $\mu = 1.381$ for $M_C = 64$, respectively.

Since the number $N_c$ of sub-carriers is typically in the order of thousands when the DVB-T standard is considered regardless of the transmission mode, the last term in (10) can be reasonably neglected and the output power level can be approximated as:

$$E\{|z[q,m]|^2|H_0, DVB-T\ case\} \cong \left\{\sum_{l=0}^{L-1} h^2[l]\right\}\eta_{LPF}\sigma_N^4\,(1+DNR)^2 \quad (11)$$

Using the same scaling strategy based on the noise factor $F = \{\sum_{l=0}^{L-1} h^2[l]\}\eta_{LPF}\sigma_N^4$, the spectrogram obtained for the DVB-T case study exhibits a background level well in line with the above prediction as it appears at $(1+DNR)^2 \cong 80\,dB$ above the reference 0 dB level (Fig. 3(d)).

As is apparent, eqs. (9) and (11) provide a theoretical demonstration of the background level increase experienced in the PFSR spectrogram when DVB-T signals are exploited compared to the case of FM radio transmissions. However, to provide further insight into the identified limitation, let us consider the signal at the output of the square modulus extractor under hypothesis $H_0$:

$$y[l]|_{H_0} = |A_D|^2|s[l]|^2 + |n[l]|^2 + 2Re\{A_D s[l]n^*[l]\} \quad (12)$$

We observe that, when FM transmissions are exploited, the first term in the r.h.s. of (12) coincides with its statistical mean value since $|s[l]|^2 = |A_s|^2 = E\{|s[l]|^2\},\ \forall l$. Therefore, at the output of the DC removal stage, this will be effectively removed and the direct signal contribution only appears in the residual cross-term (see last term in the r.h.s. of (12)). This is a direct consequence of the constant amplitude characteristic of the FM signals.

In contrast, when considering DVB-T transmissions, this characteristic does not longer hold. Therefore the DC removal stage only allows the cancellation of the mean value of the signal $|A_D|^2|s[l]|^2$ whereas an additional residual term appears with respect to the FM case due to the instantaneous non-zero difference $|A_D|^2(|s[l]|^2 - E\{|s[l]|^2\})$. This residual signal is a spectrally white process that cannot be filtered out by the LPF stage and determines the increased background level.

The considerations above are confirmed by the plot reported in Fig. 3(b) where the randomly time-varying amplitude of the exploited DVB-T signal severely masks the target induced fluctuations as the target moves away from the baseline, namely at the ends of the considered time interval. Conversely, in the FM case (see Fig. 3(a)), the square modulus extraction mostly confines the direct signal contribution to the DC component; this can be effectively suppressed by subtracting the average value thus extracting the target signature.

### C. Target Signature Fading

As observed in sub-section III.A, the target signature in the DVB-T based PFSR spectrogram has a steeper fading than that obtained for the FM based PFSR case. Actually, this is due to a combination of different effects.

Indeed, the increase in the background level discussed in the previous sub-section determines a severe masking effect on the target signature.

Also, the higher carrier frequency is responsible of a narrower pattern for the target response that basically results in a "shorter" signature with higher amplitude in the proximity of the baseline crossing point. In fact, it is easy to verify from (2) that the gain provided by the use of the DVB-T signal over the FM radio signal is about $20\log_{10}(600\text{ MHz}/100\text{ MHz}) = 15.6$ dB at the peak value of the spectrogram in the considered case study. Incidentally, we notice that this power ratio is much smaller than the increase in the background level discussed in the previous sub-section, which shows that the increase in carrier frequency cannot compensate for the undesired effect caused by the exploitation of OFDM signals of opportunity. Moreover, the target FS amplitude pattern in (2) has a narrower shape at higher carrier frequencies as the argument of the *sinc* factor is inversely dependent on the wavelength $\lambda$. This point is illustrated in Fig. 4(a-b) where the target amplitude pattern evaluated using (2) are reported in blue colour as a function of time when employing the carrier frequency corresponding to the FM radio case and the DVB-T case, respectively. The peak values have been normalized to unity in both cases. As

expected, the 1/x decay of the *sinc* sidelobes is much faster in the DVB-T case when mapped into the time axis.

The above effects certainly motivate the steeper fading of the target in Fig. 3(d) compared to Fig. 3(c). However, we notice that the target signature in the DVB-T case is further affected by an additional modulation factor that aggravates the observed decay. Therefore, in Appendix B this effect is theoretically analysed and it is shown to be caused by intrinsic characteristics of the employed waveform of opportunity.

Specifically, under the assumption that $A_T[l] \ll A_D$ and DNR>>1, the power level observed in the final spectrogram for a target along its track can be approximated as (see Appendix B):

$$P_T^{(out)}[q, \bar{m}(q)] \cong |A_D|^2 (\alpha_h[0])^2 \times \cdot |A_T[l_0 + q(L - L_{ovl})]|^2 |R_s(\tau[l_0 + q(L - L_{ovl})]|^2 \quad (13)$$

where

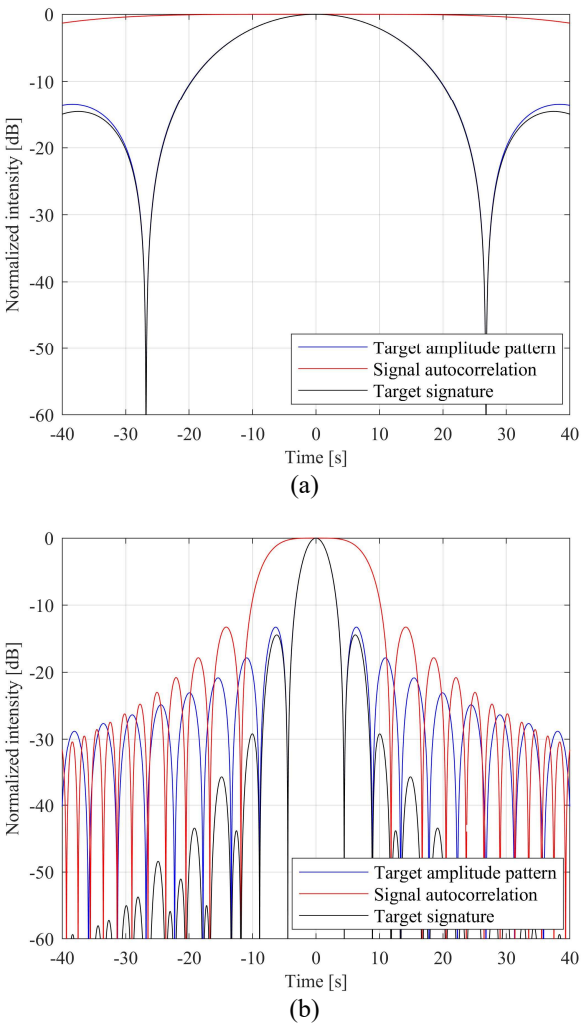


Fig. 4. Analysis of different factors affecting the target signature intensity for the FM radio case (a) and the DVB-T case (b).

- $q$ indicates the considered signal fragment, i.e. that used to evaluate the $q$-th column of the spectrogram (see eq. (8));
- $\bar{m}(q)$ is the Doppler bin where the target lies at the $q$-th signal fragment; in fact, it is assumed that the length $L$ of the considered $q$-th fragment is kept small, so that the target contribution exhibits an approximate linear phase law with slope $\bar{m}(q)$. Eq. (13) is valid for $\bar{m}(q) \neq 0$, i.e. for the sidelobes of the target signature which is the portion we are interested in (an alternative expression is provided in Appendix B for the case $\bar{m}(q)$=0).
- Similarly, we assume that the target FS amplitude in (2) and the delay in (4) are slowly varying with time so that they can be considered constant within short signal fragments, i.e. $A_T[l_0 + q(L - L_{ovl}) + l] \cong A_T[l_0 + q(L - L_{ovl})]$ and $\tau[l_0 + q(L - L_{ovl}) + l] \cong \tau[l_0 + q(L - L_{ovl})]$, $l = 0, \dots, L$. Under such conditions, the Doppler processing in (8) approximates a matched filter for target contributions.
- $\alpha_h[0] = \sum_{l=0}^{L-1} h[l]$ depends on the adopted weighting function.
- By modeling the signal $s(t)$ as a wide sense stationary stochastic complex process, the last factor in (13) is the signal autocorrelation $R_s(\tau)$ evaluated at delay $\tau = \tau[l_0 + q(L - L_{ovl}) + l]$.

According to (13), the target signature in the final spectrogram resembles the target FS amplitude pattern evaluated using (2) but it is further modulated by the autocorrelation function $R_s(\tau)$ of the signal of opportunity. The corresponding effect is greater when wider bandwidth signals are exploited since the target along its trajectory yields echoes with delays mapping into the sidelobes of the autocorrelation function. Consequently, a narrower response is observed when wider bandwidth signals are considered. This is illustrated in Fig. 4(a-b) where the autocorrelation functions are reported for the case of a FM signal and a DVB-T signal, respectively.

In both cases, under the simplifying assumption of signals modelled as spectrally white processes in the Rx bandwidth, the autocorrelation function has a *sinc* shape with main lobe width inversely proportional to the bandwidth $B_s$:

$$R_S(\tau) = sinc(\pi B_s \tau) \quad (14)$$

The results are shown as a function of time $t$, i.e. the argument of $R_s(\tau(t))$ is set to the delay $\tau(t)$ at which the target is observed at that time $t$, according to (4).

As it is apparent, the autocorrelation induced factor in (13) yields a negligible effect in the case of an FM signal of opportunity (see red curve in Fig. 4(a)). As a consequence, the overall target signature power level (black curve) is largely coincident with the curve provided by the target FS amplitude pattern. Notice that the black curve correctly describes the succession of peaks and notches in the target signature intensity of Fig. 3(c).

When a DVB-T signal is considered, a significant attenuation

This article has been accepted for publication in a future issue of this journal, but has not been fully edited. Content may change prior to final publication. Citation information: DOI 10.1109/TAES.2020.3035435, IEEE Transactions on Aerospace and Electronic Systems



results from the sidelobes of the autocorrelation function that further modulates the resulting target signature (see Fig. 4(b)). As a consequence the target contribution is likely to be buried in the background of Fig. 3(d) at times $|t| > 10\ s$.

## IV. SIGNAL-BASED BACKGROUND REDUCTION

In order to mitigate the limitations illustrated in the previous section, an innovative signal processing scheme is presented to be employed for the case of a DVB-T based PFSR.

Firstly, the background level increase is addressed in this section. As clearly demonstrated in sub-section III.B, this effect could be attributed to the amplitude modulation of the DVB-T signal that makes the DC removal stage partially ineffective since the direct signal contribution after the square modulus extraction is not confined to the DC component.

This limitation can be removed if we assume that, at the receiver side, the transmitted signal $s[l]$ is known up to a multiplicative constant:

$$x_s[l] = \alpha_s s[l] \tag{15}$$

where $\alpha_s$ is an unknown complex amplitude. In practice, when digital transmissions are employed as waveforms of opportunity, a good copy of the transmitted signal could be obtained by reconstructing the original signal from the received signal itself according to the DVB-T Standards [27][28].

Under this assumption, the signal $w[l]$ at the output of the DC removal stage can be sent in input to an additional signal-based cancellation (SBC) stage that computes:

$$\tilde{w}[l] = w[l] - \hat{\beta}\, r[l] \tag{16}$$

where

- $r[l]$ is the low-pass filtered, DC free version of the square modulus of the signal in (15), i.e. an ad hoc version of the transmitted signal transformed according to the first three stages of the processing scheme in Fig. 2, and
- $\hat{\beta}$ is an adaptive coefficient that is selected according to a least square (LS) approach in order to minimize the power of the signal at the output of the cancellation stage over a proper batch of $N_c$ samples :

$$\hat{\beta} = \underset{\beta}{\operatorname{argmin}} \left\{ \sum_{l=0}^{N_c} \tilde{w}^2[l] \right\} \tag{17}$$

which yields

$$\hat{\beta} = \frac{\sum_{l=0}^{N_c} w[l] r[l]}{\sum_{l=0}^{N_c} r^2[l]} \tag{18}$$

Eventually, the obtained signal undergoes the STFT stage which yields a modified output spectrogram indicated by $\tilde{z}[q,m]$. The new processing scheme encompassing the SBC stage is sketched in Fig. 5 where also the signal reconstruction step and its subsequent transformations are depicted.

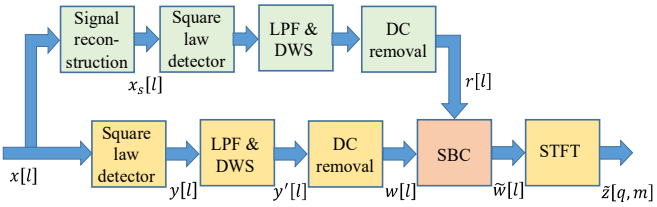


Fig. 5. DVB-T based PFSR processing scheme encompassing the SBC stage.

In Appendix C, it is shown that the proposed additional SBC stage theoretically allows to restore the background level observed in the FM radio based PFSR case. Specifically, the second moment of the generic pixel in the output spectrogram is now given by:

$$E\left\{|\tilde{z}[q,m]|^2 \ / H_0, DVB-T \,\&\, SBC\right\} = \left\{\sum_{l=0}^{L-1} h^2[l]\right\} \eta_{LPF} \sigma_N^4 \,(1 + 2\ DNR) \tag{19}$$

which coincides with (9). In fact, assuming a perfect knowledge of the transmitted signals and an asymptotic estimate of the adaptive coefficient $\hat{\beta}$, i.e. $\hat{\beta} \to \frac{|A_D|^2}{|\alpha_s|^2}$, the SBC allows to remove the randomly varying component of the signal $|A_D|^2|s[l]|^2$, not just its mean value. Therefore, under hypothesis $H_0$, the direct signal contribution only appears in a residual term, mixed with the noise contribution (see last term in the r.h.s. of (12)).

In the following we show that a significant reduction of the background level is also obtained for a finite support estimate of $\hat{\beta}$ or when using a reconstructed version of the transmitted signal, provided that the number of errors is kept small.

Notice that the SBC stage cannot substitute the DC removal stage as this is still required to remove the DC component arising from noise contribution at the output of the square-law detector. Also, we observe that the cancellation stage is not applied to the signal $x[l]$ at the input of the processing scheme in Fig. 2 as in conventional passive radar [3].

In fact, the removal of the direct signal would prevent the intrinsic PFSR capability to detect the target presence based on the amplitude modulation it produces on the signal received from the source of opportunity.

The spectrogram obtained after the application of the proposed SBC for the considered case-study is reported in Fig. 6 when assuming a perfect knowledge of both the transmitted signal and the required scaling factor. The same scaling strategy and colour scale has been adopted as in Fig. 3(c-d) to allow a direct comparison. In Fig. 6, the background level originally observed in Fig. 3(d) is correctly reduced down to the value observed for the FM case (see Fig. 3(c)). Consequently, the target signature is now visible for almost the whole of the observation period, despite its amplitude rapidly decreases when the target moves away from the baseline.

In this regard, it is interesting to observe in Fig. 7 that the peak power levels measured across consecutive time fragments in the spectrogram (red curve) perfectly trace, with a proper scaling factor, the theoretical target signature obtained as the

This article has been accepted for publication in a future issue of this journal, but has not been fully edited. Content may change prior to final publication. Citation information: DOI 10.1109/TAES.2020.3035435, IEEE Transactions on Aerospace and Electronic Systems



product of the target pattern and the signal autocorrelation factor (black curve in Fig. 7 and Fig. 4(b)).

In Fig. 8 the the output spectrograms are reported for the same case-study considered before when using different values for the DNR, i.e. DNR=40 dB, 30 dB, and 20 dB. Specifically, for each DNR value, we compare the result obtained with

(i) the conventional processing scheme in Fig. 2 (left column, 'NO SBC' label),
(ii) the modified scheme including the additional SBC that is assumed to operate with perfectly known signal and scaling coefficient (namely the ideal SBC), and
(iii) the modified scheme where the SBC exploits a sequence of transmitted symbols that is reconstructed from the received signal itself according to the DVB-T standard and an adaptive coefficient that is estimated based on (18) where the first $N_c = 1000$ samples of the observation are used.

For the sake of clarity, we point out that the first two results reported in the first row of Fig. 8 coincide with those shown in Fig. 3(d) and Fig. 6, respectively.

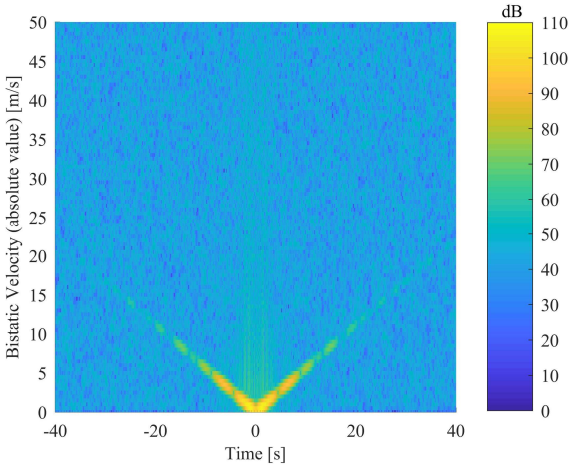


Fig. 6. Output of the PFSR processing scheme encompassing the SBC stage for the considered case-study (DNR=40 dB) when a DVB-T signal is employed and we assume a perfect knowledge of the transmitted signal and asymptotic estimate of the scaling coefficient $\hat{\beta}$.

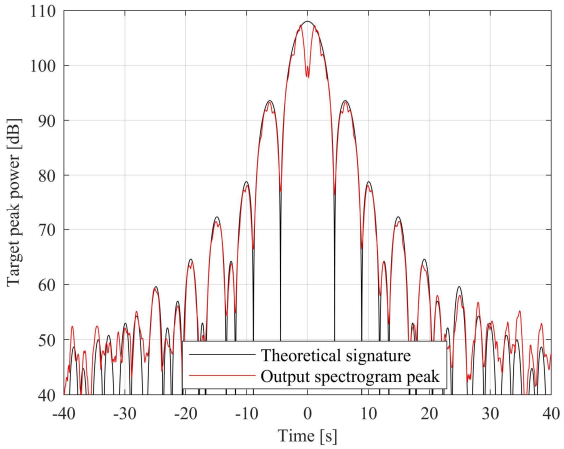


Fig. 7. Comparison of the target signature extracted from the output spectrogram and the theoretical signature obtained as the product of the target pattern and the signal autocorrelation factor.

However, in this case the colour scale adopted for the spectrograms has been limited to include an interval of about 50 dB above the minimum background level expected for each DNR value. To this purpose, the reported figures have been first scaled to the reference noise power level predicted by (19). Then the colour scale has been lower limited to a value of $DNR$ so that the minimum expected background level, namely $2 \cdot DNR$, should appear just 3 dB above the minimum of the colour scale.

The following considerations are in order:

1) With the conventional processing scheme, the background level is $DNR|_{dB}$ higher than the minimum value adopted for the colour scale, as correctly predicted by (11). This yields a severe masking effect for the target signature with all the considered DNR values (see first column of results in Fig. 8).
2) When applying the ideal SBC, the improvement is apparent in all cases since the minimum background level is always restored (see second column of results in Fig. 8). Consequently, the capability to detect the target presence enhances significantly with respect to the conventional approach, especially at higher DNR values. In fact, the improvement reduces as the DNR decreases since the target peak value scales with the direct signal power level and the signature decay determines a faster fading below the background level, although this has been reduced.
3) When the signal is reconstructed and the scaling factor $\hat{\beta}$ is adaptively estimated, the SBC is still effective for DNR=40 dB and DNR=30 dB. Specifically, the output spectrograms in the last column of Fig. 8 are almost identical to those obtained with an ideal SBC scheme. In fact, the signal reconstruction is performed with negligible errors and the estimate of the adaptive coefficient is largely comparable with its ideal value. Please notice that these DNR values can be regarded as conservative values for a typical DVB-T link budget, even assuming a noisy receiver.
4) When further reducing the DNR, the higher error probability in the demodulation stage prevents the possibility to restore the minimum background level. In addition, undesired structures appear at time fragments when burst of errors are present, which might yield false alarms. Obviously, advanced error correction strategies could be exploited to improve the signal reconstruction. However, as previously mentioned, the expected improvement for the case of DNR=20 dB is still limited due to the fast signature fading.

## V. INTEGRATED SUB-BANDS PROCESSING SCHEME

In this section the additional limitation related to the faster target signature fading is addressed and a complete signal processing scheme is presented to be effective for the case of a DVB-T based PFSR.

As clearly shown in sub-section III.C, a significant attenuation of the target signature sidelobes results from the modulating effect of the DVB-T signal autocorrelation function. Consequently, despite the SBC allows to restore the noise-limited background level, still the target contribution

This article has been accepted for publication in a future issue of this journal, but has not been fully edited. Content may change prior to final publication. Citation information: DOI 10.1109/TAES.2020.3035435, IEEE Transactions on Aerospace and Electronic Systems



might vanish below the background before expected. This effect gets worse as the DNR decreases.

In particular, as mentioned in sub-section III.C, under the simplifying assumption of signals modelled as spectrally white processes in the Rx bandwidth, the modulating autocorrelation function has a *sinc* shape with main lobe width and sidelobes separation inversely proportional to the signal bandwidth $B_s$. In other words, the PFSR processing is effective as long as the target remains within the ellipsoid corresponding to the first range gate $c/B_s$, whereas it suffers of increasing loss when the target along its path crosses consecutive ellipsoids characterized by relative bistatic ranges spaced by $c/B_s$.

On the other hand, we observe that in PFSR the discrimination and localization capability offered by the range information is intrinsically limited. In fact, the extreme bistatic geometry does not allow to preserve the range resolution offered by the exploited waveform of opportunity, which can be shown to rapidly degrade as the bistatic angle increases above 45 degrees [24]. However, in specific applications such as intrusion detection and border control, range resolution could be traded for an enhanced capability to detect the target.

Inspired by this consideration, let us consider the possibility of narrowing the signal bandwidth via pre-filtering as a way to mitigate the effect of fast target signature fading. Specifically, we assume that the signal processing scheme in Fig. 5 is applied to a band-pass filtered (BPF) version of the employed signal, being the pass-band width $B_s' = \eta_{BPF} B_s$ with $\eta_{BPF} < 1$. In this case, eqs. (13) and (19) can be easily modified as:

$$P_{T\,(BPF)}^{(out)}[q,\bar{m}(q)] \cong |A_D|^2(\alpha_h[0])^2 \times |A_T[l_0 + q(L - L_{ovl})]|^2 |R_s'(\tau[l_0 + q(L - L_{ovl})]|^2 \tag{20}$$

$$E\left\{\left|\check{z}_{(BPF)}[q,m]\right|^2 / H_0, DVB-T \,\&\, SBC\right\} = \left\{\sum_{l=0}^{L-1} h^2[l]\right\} \eta_{LPF}' \eta_{BPF}^2 \sigma_N^4 \,(1 + 2\,DNR) \tag{21}$$

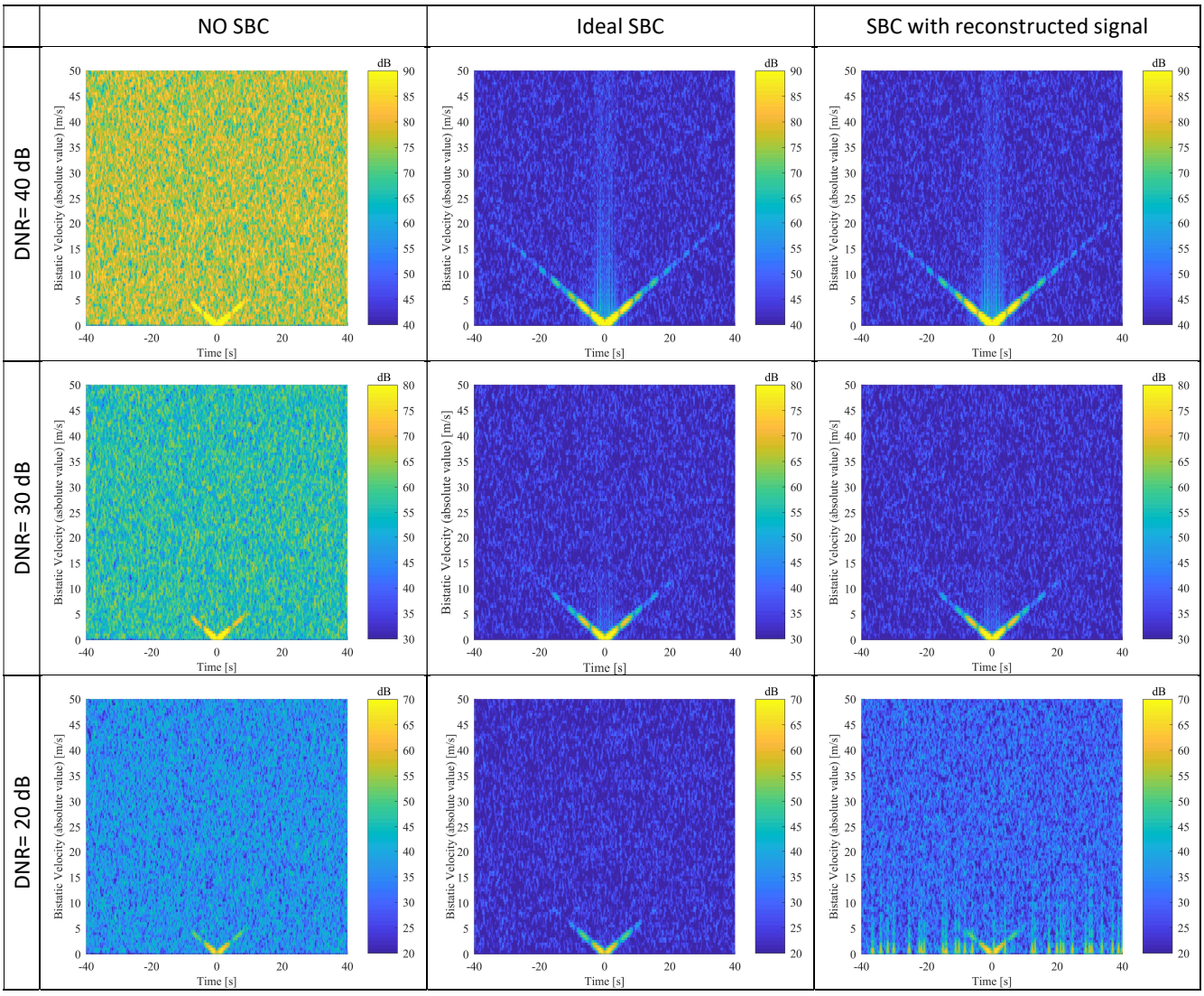


Fig. 8. Comparison of the spectrograms obtained for a DVB-T based PFSR for different values of the DNR and different processing approaches.

where the autocorrelation function $R'_S(\tau)$ in (20) accounts for the bandwidth narrowing both in terms of peak power and within the argument of the resulting *sinc* shaped response:

$$R'_S(\tau) = \eta_{BPF} sinc(\pi \eta_{BPF} B_s \tau) \quad (22)$$

In addition, the LPF coefficient in (21) is modified so that the final bandwidth and the corresponding sample rate is kept constant and independent of $\eta_{BPF}$, namely $\eta'_{LPF} = \eta_{LPF} / \eta_{BPF} = B_{LPF}/(\eta_{BPF} B_s)$.

The background level reduces by a factor $\eta_{BPF}$ with respect to the full-band case. In contrast, the target signature highest peak scales by $\eta^2_{BPF}$. However, the attenuation effect due to the modulating function $R'_S(\tau)$ is less pronounced than in the full-band case and this yields a potential advantage in the sidelobes region of the target signature, which could be observed above the background for a longer period.

This is shown in Fig. 9 where the result is reported for the considered case study with DNR=30 dB when $\eta_{BPF} = 1/4$. Specifically, the output spectrogram is reported when the processing scheme in Fig. 5 is fed with a band-pass filtered version of the received signal, namely a fourth of the original band is retained. From the direct comparison of this figure with that reported in the second row, last column of Fig. 8, we can easily verify that the target signature becomes more visible in the sidelobes region at observation times $|t| \in [12\ s, 22\ s]$.

In fact, the sidelobes decay in that region is now mostly due to the target FS amplitude pattern (blue curve in Fig. 4) since the first zero of the new autocorrelation function in (22) appears at $\tau = (\eta_{BPF} B_s)^{-1}$ that, in our case study, corresponds to observation time $|t| \cong 23.5\ s$. The zero of the modulating function is apparent in Fig. 9.

This result suggests to further reduce the signal bandwidth in order to move the first zero of the autocorrelation function to a larger distance from the baseline.

Nevertheless, this would yield an additional overall attenuation of the target pattern compared to the background level so that the advantage might become negligible. The trade-off between these two effects is illustrated in Fig. 10 where the target signature described by (20) is reported across the observation time.

Different curves are shown using different values for $\eta_{BPF}$, i.e. $\eta_{BPF} = 1$, 1/4, 1/8, 1/16, for. DNR=30 dB. The curves are scaled to the expected background level for each case, evaluated using (21), so that the result is representative of the expected signal-to-disturbance ratio. Apparently, progressively smaller values of $\eta_{BPF}$ have to be preferred as the target moves far from the baseline. However, this conclusion applies as long as the resulting curve remains well above the background level, which corresponds to the 0 dB level in each figure. In this regard, it is worth mentioning that the limiting condition largely depends on the target size and the DNR.

Aiming to mitigate the above trade-off, we observe that for a given $\eta_{BPF}$ value, a (1-$\eta_{BPF}$) portion of the available bandwidth remains unused. Therefore, the proposed approach can be extended to take further advantage of the sub-band processing scheme.

Let us assume that it is simultaneously applied against $K = 1/\eta_{BPF}$ adjacent sub-bands of the available signal, being $K$ an integer. Under the hypothesis that the signal of opportunity is spectrally white over the receiver bandwidth and further assuming that it is a narrow-band signal in terms of target response, namely the target pattern is substantially invariant across the signal band, the results obtained for the single sub-band apply unmodified for any band-pass filtered signal extracted from the set of $K$ parallel filters.

In other words, if the $K$ band-pass filtered signals separately undergo the processing scheme in Fig. 5, $K$ statistically independent spectrograms $\tilde{z}_k[q,m]$ are made available with identical characteristics both in term of disturbance contributions and target components.

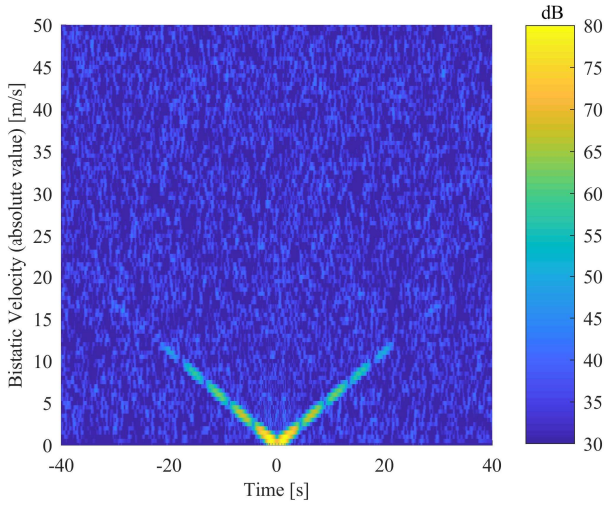


Fig. 9. Output of the PFSR scheme encompassing the SBC stage when it is fed by band-pass filtered DVB-T signal with $\eta_{BPF} = 1/4$ (DNR=30dB).

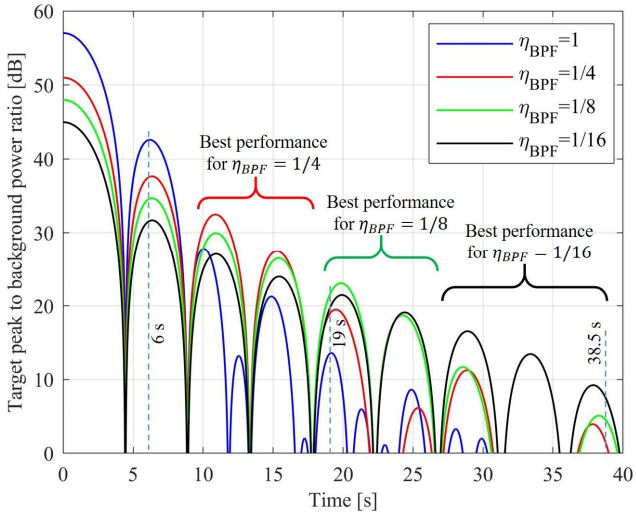


Fig. 10. Comparison of the target signatures obtained with different values of $\eta_{BPF}$ and DNR=30 dB; the curves are scaled to the expected background level for each case.

As a consequence, the sough improvement over the single-band approach can be obtained by means of a non-coherent integration of the results:

$$\zeta[q,m]=\sum_{k=0}^{K-1}|\tilde{z}_k[q,m]|^2 \tag{23}$$

which allows an effective recombination of the sub-bands.

With this approach, both the average background level and the target signature increase by $K$. However, the non-coherent integration yields a reduction of the background level fluctuation which is known to provide the expected advantage in terms of target detection capability. A sketch of the complete processing scheme of the proposed integrated sub-bands approach is shown in Fig. 11 and it will be referred to as the $K$ integrated sub-bands approach with SBC ($K$-ISB-SBC). Its performance will be extensively evaluated in the next section.

## VI. Performance Analysis

### A. Theoretical detection performance and results against simulated data

In order to measure the improvement yield by the proposed $K$-ISB-SBC scheme in term of target detection capability, we first consider the theoretical detection probability obtained with this approach as a function of the relevant parameters.

To this purpose, the probability density function (pdf) should be evaluated for the output spectrogram at each branch of the scheme in Fig. 11. In [25] it is shown that, for appropriate STFT length, namely when $L$ in (8) is sufficiently large, the pdf of the generic bin $\tilde{z}[q,m]$ of the output spectrogram can be approximated with a complex Gaussian pdf. Specifically, based on the results of this work, the corresponding random variable follows a complex normal distribution being $\tilde{z}\sim CN(\gamma A_z,\sigma_z^2)$, where $\gamma=0$ under hypothesis $H_0$ whereas $\gamma=1$ under hypothesis $H_1$. With reference to the random variables extracted at the output of each branch of Fig. 11, the variance $\sigma_z^2$ is given by (21), with $\eta_{BPF}=1/K$, whereas (20) provides the square modulus of $A_z$ along the observation time.

Consequently, the scaled output $\zeta'[q,m]=2\zeta[q,m]/\sigma_z^2$ approximately follows a central chi-square distribution under hypothesis $H_0$ and a non-central chi-square distribution under hypothesis $H_1$, i.e. $\zeta'\sim\chi'^2_{2K}(\gamma c_0)$ where $\gamma=0/1$ under hypothesis $H_0/H_1$ and the noncentrality parameter is

$$\begin{aligned}c_0&=KA_z^2\frac{2}{\sigma_z^2}\\&=\frac{2L\rho_h DNR^2}{\frac{B_{LPF}}{B_s}(1+2\,DNR)}\,|\bar{A}_T[l_0+q(L-L_{ovl})]|^2\\&\qquad\times sinc^2\left(\pi\frac{B_s}{K}\tau[l_0+q(L-L_{ovl})]\right)\end{aligned} \tag{24}$$

being $\rho_h=(\alpha_h[0])^2/\{L\sum_{l=0}^{L-1}h^2[l]\}$ the efficiency of the weighting network and $\bar{A}_T[l]=A_T[l]/A_D$ the normalized target pattern that only takes into account the system/target geometry (see (2)).

Therefore, the probability of false alarm ($P_{fa}$) can be obtained as a function of the detection threshold $\eta_0$ to be applied against the output $\zeta[q,m]$

$$P_{fa}^{(K-ISB-SBC)}=\frac{\Gamma\left(K,\frac{\eta_0}{\sigma_z^2}\right)}{\Gamma(K)}=e^{-\frac{\eta_0}{\sigma_z^2}}\sum_{k=0}^{K-1}\frac{1}{k!}\left(\frac{\eta_0}{\sigma_z^2}\right)^k \tag{25}$$

where $\Gamma(x,y)$ is the upper incomplete gamma function and $\Gamma(x)$ denotes the gamma function. Correspondingly, the detection probability ($P_d$) can be expressed as:

$$P_d^{(K-ISB-SBC)}=Q_K\left(\sqrt{c_0},\sqrt{\frac{2\eta_0}{\sigma_z^2}}\right) \tag{26}$$

where $Q_K(x,y)$ is the generalized Marcum Q-function.

The corresponding expressions can be easily obtained for the other approaches considered in this paper. Specifically, the $P_d$ for the 'X' approach is evaluated as

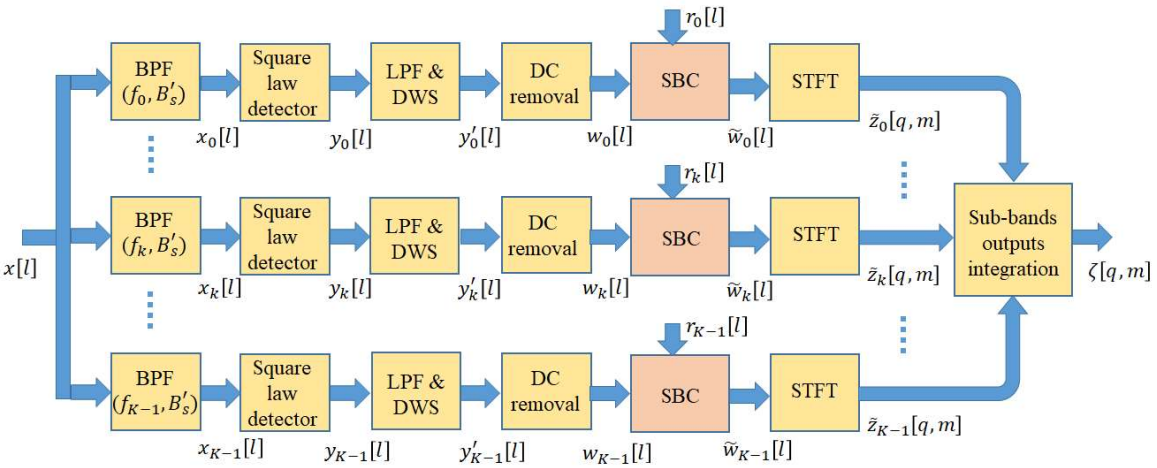


Fig. 11. Signal based integrated sub-band processing scheme for PFSR exploiting DVB-T signals.

This article has been accepted for publication in a future issue of this journal, but has not been fully edited. Content may change prior to final publication. Citation information: DOI 10.1109/TAES.2020.3035435, IEEE Transactions on Aerospace and Electronic Systems



$$P_d^{(X)} = Q_1\left(\sqrt{c_X}, \sqrt{-2lnP_{fa}}\right) \quad (27)$$

where the parameter $c_X = 2A_z^2/\sigma_z^2$ depends on the signal-to-disturbance ratio available with the considered processing scheme:

- Full-band conventional approach (FB-conv, see Fig. 2): in this case the variance $\sigma_z^2$ is given by (11) while (20) provides the square modulus of $A_z$ with $\eta_{BPF} = 1$. Therefore (27) applies with parameter

$$c_{FB-conv} = \frac{2L\rho_h DNR^2}{\frac{B_{LPF}}{B_s}(1+DNR)^2} \cdot |\bar{A}_T[l_0 + q(L - L_{ovl})]|^2 \times sinc^2(\pi B_s \tau[l_0 + q(L - L_{ovl})]) \quad (28)$$

- Full-band approach encompassing the SBC (FB-SBC, see Fig. 5): in this case the target intensity and the disturbance variance $\sigma_z^2$ are given by (20)-(21) with $\eta_{BPF} = 1$ and the parameter in (27) modifies as

$$c_{FB-SBC} = \frac{2L\rho_h DNR^2}{\frac{B_{LPF}}{B_s}(1+2\,DNR)} \cdot |\bar{A}_T[l_0 + q(L - L_{ovl})]|^2 \times sinc^2(\pi B_s \tau[l_0 + q(L - L_{ovl})]) \quad (29)$$

- Sub-band approach encompassing the SBC (SB-SBC, see Fig. 5 when fed with a band-pass filtered signal): in this case the target intensity and the disturbance variance $\sigma_z^2$ are given by (20)-(21) with $\eta_{BPF} < 1$ and the relevant parameters is evaluated as

$$c_{SB-SBC} = \frac{2\eta_{BPF} L\rho_h DNR^2}{\frac{B_{LPF}}{B_s}(1+2\,DNR)} \cdot |\bar{A}_T[l_0 + q(L - L_{ovl})]|^2 \times sinc^2(\pi\eta_{BPF} B_s \tau[l_0 + q(L - L_{ovl})]) \quad (30)$$

The theoretical $P_d$ curves obtained using (26) and (27) with parameters as in (28)-(30) are reported in Fig. 12(a-c) for the case study under consideration, with $P_{fa} = 10^{-6}$ and $K$=16. The results are reported as functions of the DNR at three different observation times: (a) at 6 s; (b) at 19 s; (c) at 38.5 s. The selected time instants are indicated with vertical dashed lines in Fig. 10 in order to highlight the impact of the target signature sibelobe structure made available with different approaches. The observation time at 6 s corresponds to the case where a FB-SBC approach provides the highest sidelobe structure; in contrast, at observations times equal to 19 s and 38.5 s, a sub-band approach could be preferred provided that the available target signature remains well above the disturbance background.

As regards the full band approaches, the curves in Fig. 12 largely confirms the results of Fig. 8. Specifically, the conventional FB processing scheme (dashed blue line) does not allow to detect the considered target over long observation times regardless of the DNR (see Fig. 12(b-c)).

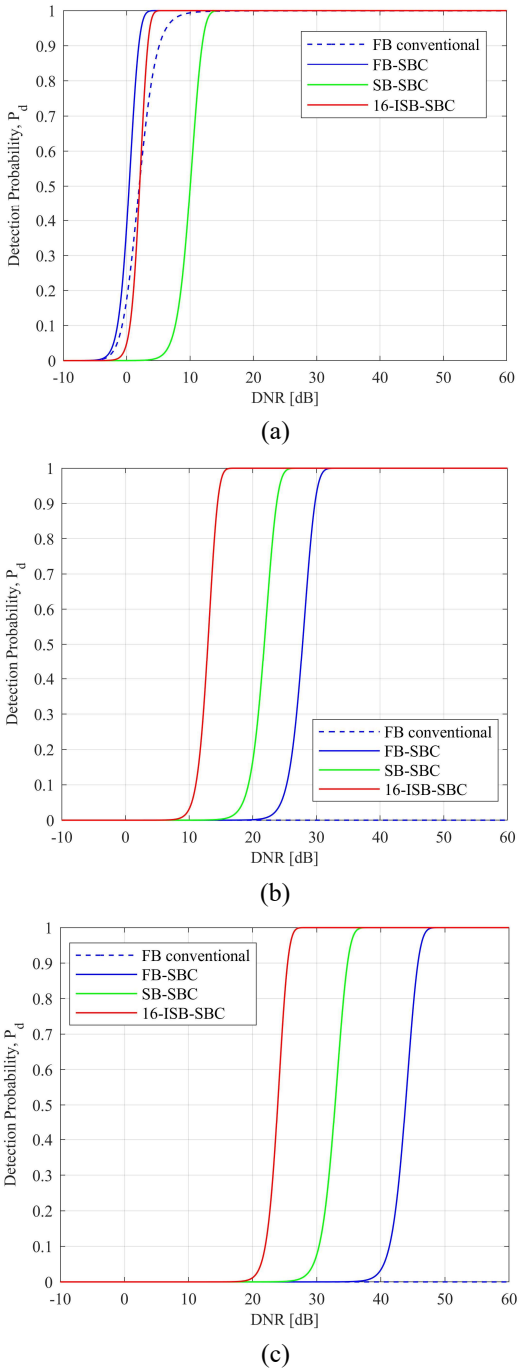


Fig. 12. Target detection probability versus DNR obtained for the case study under consideration with full-band and sub-band approaches along the observation time: (a) at 6 s; (b) at 19 s; (c) at 38.5 s.

When applying the proposed SBC approach, the resulting FB-SBC (solid blue line) is able to detect the target as it moves far from the baseline, provided that the DNR is high enough to compensate for the target amplitude fading due to the signal autocorrelation.

Operating with a SB-SBC approach with $\eta_{BPF} = 1/16$ (green line) degrades the performance in the proximity of the baseline crossing point (Fig. 12(a)) whereas it yields substantial improvement over the FB-SBC at subsequent observation times (Fig. 12(b-c)).

This article has been accepted for publication in a future issue of this journal, but has not been fully edited. Content may change prior to final publication. Citation information: DOI 10.1109/TAES.2020.3035435, IEEE Transactions on Aerospace and Electronic Systems



The proposed *K*-ISB-SBC (red line) yields the best performance since

- it only shows a limited loss w.r.t. the FB-SBC at small observation times (Fig. 12(a)) where the detection performance is remarkable with all the considered approaches;
- it provides tremendous improvement over the FB-SBC at subsequent observation times showing that the non-coherent integration across the *K*=16 available sub-bands allows to retain the benefits of the SB approach while recovering for the inherent power loss. This allows the target to be detected at larger distances from the baseline even operating with a limited DNR value.

In this regard, we recall that this theoretical performance analysis does not take into account the errors in the signal reconstruction which might jeopardize the performance at low DNR values.

Ideally, the value of *K* could be increased to further extend the coverage. However, this would be paid in terms of computational load as *K* parallel processing chains have to be implemented. Moreover, the practical advantage of further increasing *K* might become negligible when the target amplitude fading due to its FS response becomes the limiting factor or when the receiver antenna beampattern results in the tightest constraint.

The detection results obtained for the case study under consideration with DNR=30 dB are reported in Fig. 13 when applying different processing schemes and corresponding thresholds. Specifically, Fig. 13(a-d) are respectively for the conventional FB processing scheme, the FB-SBC approach, the SB-SBC approach with $\eta_{BPF} = 1/16$, and the *K*-ISB-SBC scheme with *K*=16. In each figure a b/w color scale is used to indicate bins where a detection is declared, namely where the measured amplitude exceeds the threshold, which was set to guarantee a nominal $P_{fa} = 10^{-6}$.

The performed comparison confirms the theoretical results of the previous sub-section and clearly demonstrates that an increasingly earlier detection of the target can be obtained by jointly exploiting the proposed approaches.

Please notice that, in this case, the SBC is applied based on the available reconstruction of the transmitted signal, which was shown to be quite effective for DNR higher than 20 dB.

The sole application of the SBC to the full-band signal allows to double the observation time during which the target is correctly detected (see Fig. 13(b)).

The 16-ISB-SBC scheme provides a continuous detection capability along the whole observation time with missed detections only due to the zeros of the target amplitude pattern. In this regard, the combination of the results obtained at different DVB-T broadcast channels might provide the required frequency diversity in order to counteract this effect.

It is interesting to observe that the use of a simpler SB-SBC scheme largely improves the performance with respect to the conventional processing scheme and can be regarded as an effective lower cost approach for this particular case study where the target response peak level can be traded for a wider FS signature.

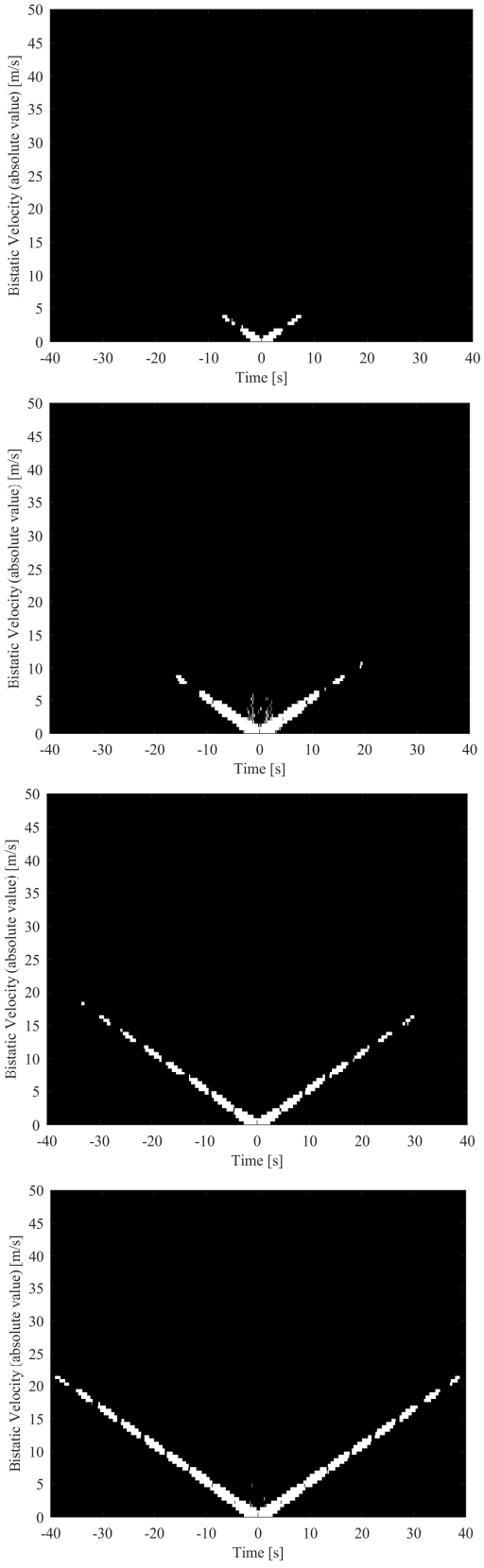


Fig. 13. Comparison of the detection results for the considered case study when using different approaches with $P_{fa}=10^{-6}$ and DNR=30dB: (a) Conventional processing scheme (FB, no SBC); (b) FB-SBC; (c) SB-SBC with $\eta_{BPF} = 1/16$; (d) *K*-ISB-SBC with K=16 sub-bands.

However, this is not always the case if additional losses are experienced such as those arising from the vertical FS response of the target (e.g. for target flying above the baseline [14]) or when small size targets are considered.

### *B. Application to experimental data*

In this sub-section, the results are reported against an experimental dataset collected by a COTS based receiver fielded at Sapienza University of Rome. The acquisition geometry is illustrated Fig. 14 where the positions of the Rx and the Tx of opportunity are clearly indicated along with the trajectory of the target, a Boeing 737-800, landing at the Ciampino airport of Rome. Additional details about the experimental test and the target of opportunity are listed in Table III. Moreover, the instantaneous bistatic velocity, the relative bistatic range, and the altitude of the target along the acquisition time are reported in Fig. 15, as provided by a commercial ADS-B receiver.

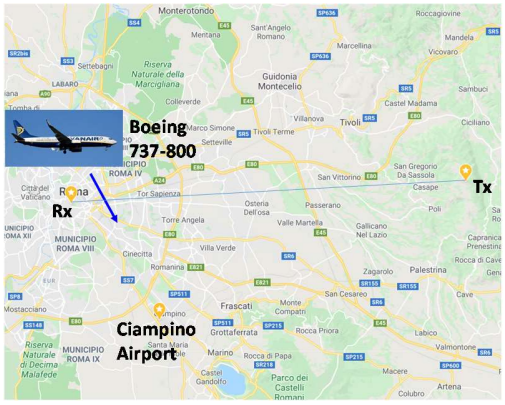


Fig. 14. Acquisition geometry for the experimental test. Map data ©2020 Google.

TABLE III
EXPERIMENTAL TEST DETAILS

| Description | Symbol | Value |
|---|---|---|
| *Tx and Rx parameters* | | |
| Carrier frequency | $f_c$ | 482 MHz |
| DVB-T tx mode | | 8k, GI 1/4, 64-QAM |
| Signal bandwidth | $B_s$ | 7.62 MHz |
| Tx-Rx Baseline | $B$ | 36.1 km |
| Direct signal to noise Ratio (estimated) | DNR | ~20 dB |
| Sampling frequency | $f_s$ | 64/7 MHz |
| Acquisition duration | | ~37 s |
| *Target parameters* | | |
| Target size | | Length 39.5m, Height 12.5m, Wing span 34.3m |
| Target speed | v | 102 m/s (average) |
| Crossing point | $R_R$ | 3.1 km |
| Incidence angle | $\phi$ | 66.3 deg |

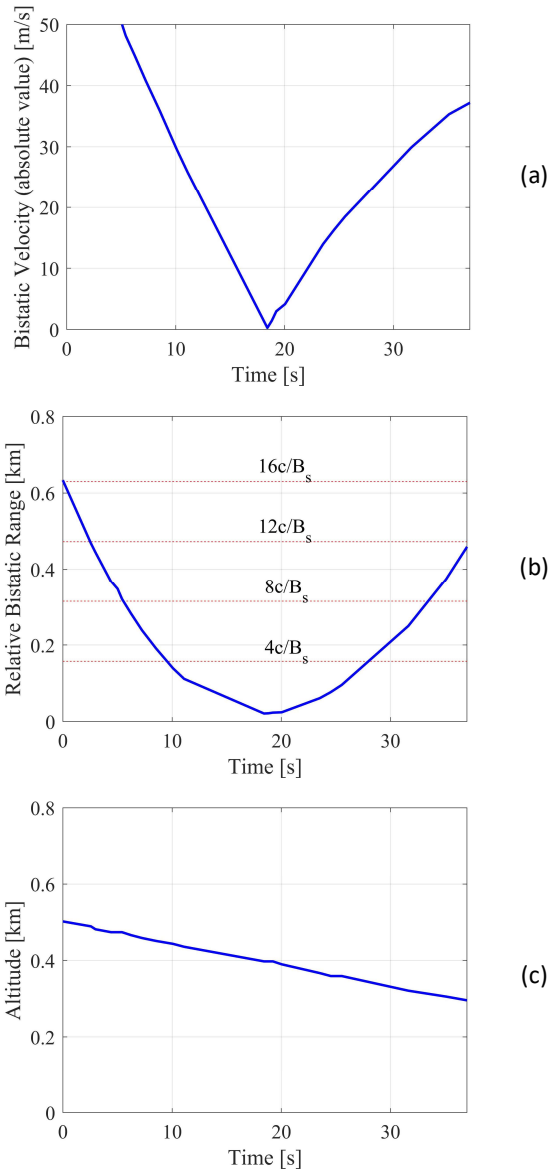


Fig. 15. Instantaneous coordinates of the target of opportunity: (a) bistatic velocity; (b) relative bistatic range; (c) altitude.

As is apparent, the target along its path crosses consecutive ellipsoids characterized by relative bistatic ranges multiple of the range resolution $c/B_s$. Therefore, it is expected that a conventional PFSR processing suffers of significant loss.

This is shown in Fig. 16 where the results are reported for different processing schemes using the same parameters adopted for the simulated case study.

Specifically, Fig. 16(a-c) show the output spectrograms for a FB approach, a SB approach with $\eta_{BPF} = 1/16$, and a $K$-ISB with $K$=16, all operating without a SBC stage. The results of the corresponding processing schemes encompassing the SBC stage are reported in Fig. 16(d-f). As for the simulated analysis, all the figures have been scaled to the estimated noise floor.

As is apparent, the FB conventional processing scheme only allows to reveal the target presence when it is very close to the

This article has been accepted for publication in a future issue of this journal, but has not been fully edited. Content may change prior to final publication. Citation information: DOI 10.1109/TAES.2020.3035435, IEEE Transactions on Aerospace and Electronic Systems



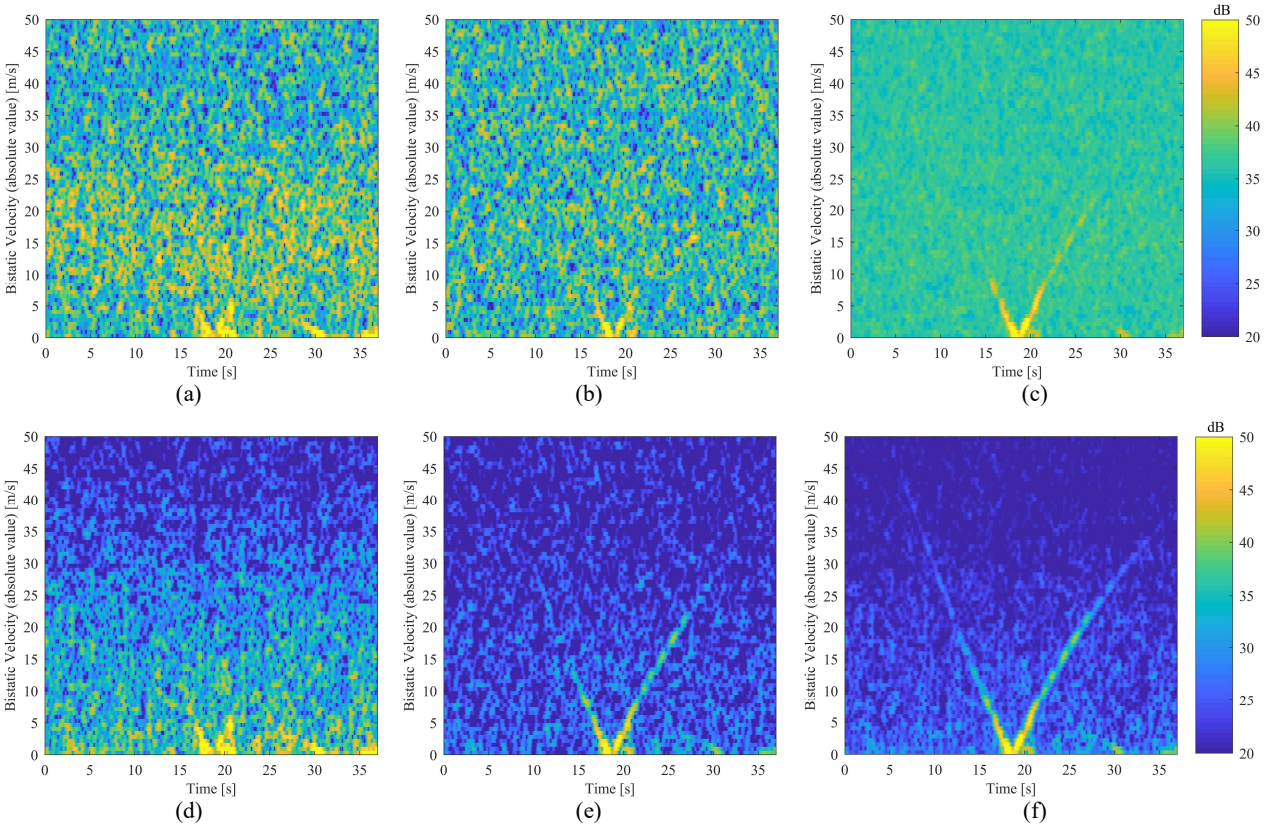


Fig. 16. Comparison of the results obtained against experimental data when using different approaches: (a) FB, no SBC; (b) SB with $\eta_{BPF} = 1/16$, no SBC; (c) *K*-ISB with K=16, no SBC, (d) FB-SBC; (e) SB-SBC with $\eta_{BPF} = 1/16$; (f) *K*-ISB-SBC with K=16.

baseline (Fig. 16(a)). This is partly due to the target altitude above the baseline that limits the FS response perceived at the receiver [14]. However, the fading effect is mostly caused by the signal autocorrelation properties and the severe background, which appears about $2 \times DNR\ [dB] = 40\ dB$ above the nominal noise level.

The former effect can be mitigated by operating at single sub-band level (see Fig. 16(b)) or by recombining the results at multiple sub-bands (see Fig. 16(c)). However, despite the expected widening of the target response, the severe background still prevents the target detection far from the baseline crossing point. Nevertheless, in Fig. 16(c) the target contribution is apparent for a much larger time interval, at least at one side of the 'V-shaped' signature. The imbalance of the target amplitude at the two branches of its signature can be explained based on the altitude pattern of the landing aircraft (see Fig. 15(c)).

This analysis also highlights the key role played by the SBC stage (see Fig. 16(d-f)). Specifically, the SBC allows to largely reduce the background level especially at high Doppler frequencies. The residuals at low Doppler frequencies especially evident in the case of a FB-SBC approach (see Fig. 16(d)) can be attributed to multipath contributions and reference signal reconstruction errors, as expected for the estimated DNR level of 20 dB. This is also confirmed by the improved effectiveness of the SBC when applied against a single sub-band of the original signal (see Fig. 16(e)). In fact, when operating against a narrow portion of the OFDM band, it is expected that the propagation channel effect is reduced together with the number of decoding errors occurred, assuming that these are equally distributed at different sub-carriers.

As in the simulated case-study, the combination of a SB approach and the SBC stage allows a tremendous improvement of the achievable performance being the target signature visible for most of the observation time. Specifically, the target is now observed beyond the FS pattern main lobe and first sidelobes.

The advantage further enhances when using the K-ISB-SBC processing scheme, especially at high bistatic velocity where the background fluctuation is effectively mitigated and the target signature benefits from the integration across sub-bands.

## VII. Conclusions

In this paper, the use of OFDM modulated DVB-T signals has been investigated as waveforms of opportunity for passive forward scatter radar.

The limitations of conventional signal processing schemes have been studied by means of theoretical, simulated, and experimental analyses and appropriate signal-dependent solutions have been proposed to enable an effective operation of the resulting PFSR system exploiting digital television broadcast transmitters. The advantages of the proposed solutions are apparent when applied to both simulated and

experimental data if the $DNR$ is not significantly degraded. These advantages are shown to provide enhanced surveillance capability to the resulting system.

Whilst the limitations above have been specifically addressed for the case of DVB-T signals, the underlying motivations and proposed solutions might be easily extended to several waveforms of opportunity exploited in PFSR applications (e.g. DAB, LTE, etc.). Therefore, the proposed approaches are expected to improve the performance of a multi-band PFSR system that exploits a dense network of diverse illuminators of opportunity.

Future activities will include dedicated analyses aimed at understanding the impact of multipath on the proposed approaches.

## APPENDIX A
## EVALUATION OF THE OUTPUT DISTURBANCE POWER LEVEL

This Appendix provides mathematical evaluation of the first and second moments of the random variable extracted at the generic pixel of the output spectrogram $z[q,m]$ in the absence of target, i.e. under hypothesis $H_0$. To this purpose, it is assumed that the input signal undergoes the processing scheme illustrated in Section II.B.

Based on (8), we can write for the first moment:

$$E\{z[q,m]|H_0\} = \sum_{l=0}^{L-1} h[l] e^{-\frac{j2\pi ml}{L}} \times E\{w[l_0 + q(L - L_{ovl}) + l]|H_0\} = 0 \quad (31)$$

since, according to (7),

$$E\{w[l]|H_0\} = E\{y'[l] - \overline{y'[l]}|H_0\} = 0 \quad (32)$$

where it is assumed that the average value of the signal $y'[l]$ evaluated over an appropriate temporal interval $T_{DC}$ is an unbiased estimator of its statistical mean value. The result above is independent of the employed waveform of opportunity.

The second moment can be then evaluated as

$$E\{|z[q,m]|^2|H_0\} = \sum_{l=0}^{L-1}\sum_{p=0}^{L-1} h[l]h[p]\, e^{-\frac{j2\pi m(l-p)}{L}} \times E\{w[l_0 + q(L - L_{ovl}) + l]w[l_0 + q(L - L_{ovl}) + p]|H_0\} \quad (33)$$

Therefore, we need to evaluate the autocorrelation of the process $\{w[l]\}$. To this purpose, we recall that the employed waveform is modelled as a wide-sense stationary process, spectrally white over the receiver bandwidth. Therefore we have $E\{s[l]s^*[p]\} = \delta[l-p]$, where a unitary power signal is considered and $\delta[m]$ is the Kronecker delta. As a consequence, at the output of the instantaneous non-linearity that extracts the square modulus we can write:

$$E\{y[l]|H_0\} = E\{|x[l]|^2|H_0\} = |A_D|^2 + \sigma_N^2 \quad (34)$$

and

$$E\{y[l]y[p]|H_0\} = E\{|x[l]|^2|x[p]|^2|H_0\} = \left[|A_D|^4(m_{s,4} - 1) + \sigma_N^4 + 2|A_D|^2\sigma_N^2\right]\delta[l-p] + (|A_D|^2 + \sigma_N^2)^2 \quad (35)$$

where $m_{s,4} = E\{|s[l]|^4\}$. Eqs. (34)-(35) clearly show that the process $\{y[l]\}$ is the superposition of a spectrally white process and a DC component.

The LPF and down-sampling stage in Fig. 2 do not modify the DC component; in contrast, assuming that the LPF has a frequency response that is approximately rectangular in the bandwidth of interests, the narrowing of the power spectral density can be taken into account by proportionally reducing the process variance. Therefore, we obtain:

$$E\{y'[l]|H_0\} = |A_D|^2 + \sigma_N^2 \quad (36)$$

$$E\{y'[l]y'[p]|H_0\} = \eta_{LPF}\left[|A_D|^4(m_{s,4} - 1) + \sigma_N^4 + 2|A_D|^2\sigma_N^2\right]\delta[l-p] + (|A_D|^2 + \sigma_N^2)^2 \quad (37)$$

By proceeding further, at the output of the DC removal stage, we can write:

$$E\{w[l]w[p]/H_0\} = \eta_{LPF}\left[|A_D|^4(m_{s,4} - 1) + \sigma_N^4 + 2|A_D|^2\sigma_N^2\right]\delta[l-p] \quad (38)$$

that can be substituted into (33) to obtain:

$$E\{|z[q,m]|^2|H_0\} = \left\{\sum_{l=0}^{L-1} h^2[l]\right\} \times \eta_{LPF}\left[|A_D|^4(m_{s,4} - 1) + \sigma_N^4 + 2|A_D|^2\sigma_N^2\right] \quad (39)$$

The final result depends on the particular waveform adopted via the fourth moment $m_{s,4}$.

In particular, for a FM radio transmission, we have

$$m_{s,4}^{(FM)} = E\{|s[l]|^4\} = A_s^4 = 1 \quad (40)$$

where $A_s$ is the constant amplitude of the FM radio transmission. This yields

$$E\{|z[q,m]|^2|H_0, FM\ case\} = \left\{\sum_{l=0}^{L-1} h^2[l]\right\}\eta_{LPF}\sigma_N^4[1 + 2\,DNR] \quad (41)$$

In contrast, when a DVB-T signal is used, with the positions illustrated in Section III.A, the variance $\sigma_s^2$ of the signal, assumed unitary in this paper, can be expressed as

$$m_{s,2}^{(DVBT)} = \sigma_s^2 = 1 = E\{|s[l]|^2\} = E\left\{\left|\sum_{p=0}^{N_c-1} d_l[p]\, \mathrm{e}^{j2\pi\frac{pl}{N_c}}\right|^2\right\} = \sum_{p=0}^{N_c-1} E\{|d_l[p]|^2\} = N_c C \quad (42)$$

where $d_l[p]$ is the constellation symbol transmitted at time $l$ using the $p$-th sub-carrier ($p$=0,.., $N_c-1$) and $C$ is defined in Section III.B. Therefore, in this paper we assume that the constellation is scaled so that $C = 1/N_c$.

Correspondingly, the fourth moment is evaluated as

$$m_{s,4}^{(DVBT)} = \left\{\left|\sum_{p=0}^{N_c-1} d_l[p]\, \mathrm{e}^{j2\pi\frac{pl}{N_c}}\right|^4\right\} = C^2 \sum_{p=0}^{N_c-1} E\left\{\frac{|d_l[p]|^4}{C^2}\right\} + 2\,N_c C\,(N_c-1)C = \frac{\mu-2}{N_c} + 2 \quad (43)$$

where $\mu = \frac{1}{M_C}\sum_{p=0}^{M_C-1}\frac{|c_p|^4}{C^2}$ is dependent on the adopted modulation scheme.

As a consequence, the output power level is written as:

$$E\{|z[q,m]|^2|H_0, DVB-T\ case\} = \left\{\sum_{l=0}^{L-1} h^2[l]\right\}\eta_{LPF}\sigma_N^4\left[[1+DNR]^2 + DNR^2\left(\frac{\mu-2}{N_c}\right)\right] \quad (44)$$

## APPENDIX B
## EVALUATION OF THE OUTPUT TARGET POWER LEVEL

This Appendix provides mathematical evaluation of the target peak power level at the output spectrogram $z[q,m]$ when employing the signal processing scheme illustrated in Section II.B.

Specifically, we evaluate the target peak power at the output spectrogram for the $q$-th CPI as

$$P_T^{(out)}[q,\bar{m}(q)] = |E\{z[q,\bar{m}(q)]|H_1\}|^2 \quad (45)$$

being $\bar{m}(q)$ the Doppler bin where the target energy is maximally focused at the $q$-th fragment. Therefore we need to evaluate

$$E\{z[q,m]|H_1\} = \sum_{l=0}^{L-1} h[l]e^{-\frac{j2\pi ml}{L}} \times E\{w[l_0+q(L-L_{ovl})+l]|H_1\} \quad (46)$$

Under hypothesis $H_1$, we can easily write the signal at the output of the DC removal stage as:

$$\begin{aligned} w[l]|_{H_1} = LPF\{&(|A_D|^2|s[l]|^2 - |A_D|^2) + (|n[l]|^2 - \sigma_N^2) \\ &+2\mathrm{Re}\{A_D^* s[l]n[l]\} + 2\mathrm{Re}\{A_D^* s^*[l]A_T[l]e^{j\varphi[l]}\, s^{(\tau[l])}[l]\} \\ &+ |A_T[l]|^2\left|s^{(\tau[l])}[l]\right|^2 + 2\mathrm{Re}\{A_T^*[l]e^{j\varphi[l]}\, s^{(\tau[l])}[l]n^*[l]\}\} \end{aligned} \quad (47)$$

where $LPF\{x[l]\}$ indicates the low-pass filtered and down-sampled version of the signal $x[l]$. Assuming that $A_T[l] \ll A_D$ and DNR>>1, the last two target contributions could be assumed to be negligible w.r.t. other terms in the sum.

Therefore, the expression above can be approximated as:

$$w[l]|_{H_1} \cong w[l]|_{H_0} + LPF\left\{2Re\{A_D^* s[l]A_T[l]e^{j\varphi[l]}\, s^{(\tau[l])}[l]\}\right\} \quad (48)$$

where $w[l]|_{H_0}$ collects all the contributions obtained under hypothesis $H_0$ and the target response is encoded in the second term.

By observing that the LPF operation does not affect the mean value of the signal in (47) and, based on (32), $\mathrm{E}\{z[q,\bar{m}(q)]|H_0\} = 0$, we can evaluate (46) as:

$$E\{z[q,m]|H_1\} = 2|A_D|\sum_{l=0}^{L-1} h[l]e^{-\frac{j2\pi ml}{L}} \times \mathrm{Re}\left\{e^{j(\varphi[l_0+q(L-L_{ovl})+l]-\varphi_D)} \cdot A_T[l_0+q(L-L_{ovl})+l] \cdot E\{C_s[l,l_0,q]\}\right\} \quad (49)$$

where we factorized $A_D$ as $A_D = |A_D|e^{j\varphi_D}$ and we posed for brevity:

$$C_s[l,l_0,q] = s^*[l_0+q(L-L_{ovl})+l] \cdot s^{(\tau[l_0+q(L-L_{ovl})+l])}[l_0+q(L-L_{ovl})+l] \quad (50)$$

Notice that, with the definition in (50) and recalling that we modeled the signal $s(t)$ as a wide sense stationary stochastic complex process, the last factor within the summation in (49) can be expressed as:

$$E\{C_s[l,l_0,q]\} = R_s(\tau[l_0+q(L-L_{ovl})+l]) \quad (51)$$

being $R_s(\tau)$ the signal statistical autocorrelation evaluated at delay $\tau$.

As mentioned in Section II.B, if the length $L$ of the considered $q$-th fragment is kept small, the STFT in (8) approximates a matched filter for target contribution that appears as nearly constant in amplitude and delay and linearly varying in phase over short CPIs, i.e.

$$\begin{cases} A_T[l_0+q(L-L_{ovl})+l] \cong A_T[l_0+q(L-L_{ovl})] \\ \tau[l_0+q(L-L_{ovl})+l] \cong \tau[l_0+q(L-L_{ovl})] \\ \varphi[l_0+q(L-L_{ovl})+l] \cong 2\pi\bar{m}(q)l/L + \varphi_0[q] \end{cases} \quad (l=0,\dots,L) \quad (52)$$

where $\varphi_0[q]$ is a constant phase term across the $q$-th fragment.

With the positions in (52), we also have:

$$R_s(\tau[l_0 + q(L - L_{ovl}) + l]) \cong R_s(\tau[l_0 + q(L - L_{ovl})]) \quad (53)$$

which depends on the 2-way delay of the target echo with respect to the direct signal at the $q$-th signal fragment.

Under the assumptions above, the target peak power is written as:

$$P_T^{(out)}[q, \bar{m}(q)] = 4|A_D|^2 \times \left| \sum_{l=0}^{L-1} h[l] e^{-\frac{j2\pi\bar{m}(q)l}{L}} \mathrm{Re}\left\{ e^{j(2\pi\bar{m}(q)l/L + \varphi_0[q] - \varphi_D)} \cdot A_T[l_0 + q(L - L_{ovl})] \cdot R_s(\tau[l_0 + q(L - L_{ovl})]) \right\} \right|^2 \quad (54)$$

Consequently, we can further develop (54) as:

$$P_T^{(out)}[q, \bar{m}(q)] = |A_D|^2 \left| e^{j(\varphi_0[q] - \varphi_D)} A_T[l_0 + q(L - L_{ovl})] \cdot R_s(\tau[l_0 + q(L - L_{ovl})]\, \alpha_h[0] + e^{-j(\varphi_0[q] - \varphi_D)} A_T^*[l_0 + q(L - L_{ovl})] \cdot R_s^*(\tau[l_0 + q(L - L_{ovl})] \alpha_h[\bar{m}(q)] \right|^2 \quad (55)$$

where we have defined

$$\alpha_h[m] = \sum_{l=0}^{L-1} h[l]\, e^{-j\frac{4\pi ml}{L}} \quad (56)$$

We observe that, in the absence of a weighting function, i.e. for $h[l] = 1 \ \forall l, \quad \alpha_h[m] \neq 0$ only for $m \neq 0$. Anyway, if an appropriate network is employed to limit the sidelobes level of the Doppler response in the final spectrogram, $\alpha_h[m]$ would exactly represent the value of such response at Doppler bin $2m$. Consequently, the second additive term within the square modulus of (55) corresponds to the contribution from the low sidelobes of the target echo component symmetrical about the zero Doppler (we recall that we are evaluating the spectrogram of a real input signal).

Therefore, by neglecting this contribution for target lying in the $\bar{m}(q)$-th Doppler bin we obtain:

- $for\ \bar{m}(q) = 0$:

$$P_T^{(out)}[q, \bar{m}(q)] = 4|A_D|^2 (\alpha_h[0])^2 \cdot \left| \mathrm{Re}\left\{ e^{j(\varphi_0[q] - \varphi_D)} A_T[l_0 + q(L - L_{ovl})] \cdot R_s(\tau[l_0 + q(L - L_{ovl})] \right\} \right|^2 \quad (57)$$

- $for\ \bar{m}(q) \neq 0$:

$$P_T^{(out)}[q, \bar{m}(q)] \cong |A_D|^2 (\alpha_h[0])^2 \cdot |A_T[l_0 + q(L - L_{ovl})]|^2 |R_s(\tau[l_0 + q(L - L_{ovl})]|^2$$

## APPENDIX C
### OUTPUT DISTURBANCE POWER LEVEL AFTER SBC

This Appendix provides mathematical evaluation of the first and second moments of the random variable extracted at the generic pixel of the output spectrogram $\tilde{z}[q, m]$, in the absence of target, i.e. under hypothesis $H_0$. To this purpose, it is assumed that the input signal undergoes the processing scheme described in Section IV, there including the SBC additional cancellation stage.

Under hypothesis $H_0$, starting from (47), we can write the signal $w[l]$ at the output of the DC removal stage as follows:

$$w[l]|_{H_0} = LPF\{(|A_D|^2 |s[l]|^2 - |A_D|^2) + (|n[l]|^2 - \sigma_N^2) + 2\mathrm{Re}\{A_D^* s[l] n[l]\} \quad (58)$$

whose mean value and variance are described in (32) and (38), respectively. As is apparent, $w[l]|_{H_0}$ is the sum of three uncorrelated processes:

$$w[l]|_{H_0} = |A_D|^2 \nu_s[l] + \nu_n[l] + \nu_d[l] \quad (59)$$

where the following zero-mean wide-sense stationary processes are defined, which are spectrally white over the receiver bandwidth:

$$\begin{aligned} \nu_s[l] &= LPF\{|s[l]|^2\} - 1 \\ \nu_n[l] &= LPF\{|n[l]|^2\} - \sigma_N^2 \\ \nu_d[l] &= 2\mathrm{Re}\{A_D^* s[l] n[l]\} \end{aligned} \quad (60)$$

with variances $\eta_{LPF}(m_{s,4} - 1)$, $\sigma_N^4$, and $2\eta_{LPF}|A_D|^2\sigma_N^2$, respectively. Specifically, we observe that $\nu_s[l]$ encodes the random fluctuation that is responsible of the background level increase when using DVB-T signals as waveforms of opportunity.

Similarly, the signal $r[l]$ defined in (16), can be written as

$$r[l] = |\alpha_s|^2 \nu_s[l] \quad (61)$$

$\alpha_s$ being an unknown complex amplitude.

With the positions above, the adaptive coefficient in (18) provides an unbiased estimate and asymptotically converges to the amplitude ratio of the components proportional to $\nu_s[l]$ in (59) and (61). In other words we have $E\{\hat{\beta}\} = |A_D|^2/|\alpha_s|^2$ and

$$\hat{\beta} = \frac{\sum_{l=0}^{N_c} w[l] r[l]}{\sum_{l=0}^{N_c} (r[l])^2} \xrightarrow[N_c \to \infty]{} \frac{E\{w[l] r[l] | H_0\}}{E\{r^2[l]\}} = \frac{|A_D|^2}{|\alpha_s|^2} \quad (62)$$

since, based on (59)-(61), it can be easily verified that $E\{w[l] r[l] | H_0\} = |A_D|^2 |\alpha_s|^2 \eta_{LPF}(m_{s,4} - 1)$ and $E\{r^2[l]\} = |\alpha_s|^4 \eta_{LPF}(m_{s,4} - 1)$.

At the output of the SBC we have

$$E\{\widetilde{w}[l]|H_0\} = E\{w[l] - \hat{\beta}r[l]\big|H_0\} = 0 \tag{63}$$

and

$$\begin{aligned} E\{\widetilde{w}^2[l]|H_0\} = \\ E\{w^2[l]|H_0\} + \hat{\beta}^2 E\{r^2[l]|H_0\} \\ - 2\hat{\beta}E\{w[l]r[l]|H_0\} \end{aligned} \tag{64}$$

Based on (62), the signal output power in (64) asymptotically converges to its minimum value given by

$$\begin{aligned} E\{\widetilde{w}^2[l]|H_0\} &= E\{w^2[l]|H_0\} - \frac{[E\{w[l]r[l]|H_0\}]^2}{E\{r^2[l]\}} \\ &= \eta_{LPF}\left[|A_D|^4(m_{s,4}-1) + \sigma_N^4 + 2|A_D|^2\sigma_N^2\right] \\ &\quad - \frac{\left[|A_D|^2|\alpha_s|^2\eta_{LPF}(m_{s,4}-1)\right]^2}{|\alpha_s|^4\eta_{LPF}(m_{s,4}-1)} \\ &= \eta_{LPF}[\sigma_N^4 + 2|A_D|^2\sigma_N^2] \end{aligned} \tag{65}$$

where the effect of the SBC is clearly apparent.

The second moment of the output spectrogram can be then evaluated as

$$\begin{aligned} &E\{|\tilde{z}[q,m]|^2|H_0,\ DVB-T\ \&\ SBC\} \\ &= \sum_{l=0}^{L-1} h^2[l]\, E\{\widetilde{w}^2[l_0 + q(L - L_{ovl}) + l]|H_0\} \\ &= \left\{\sum_{l=0}^{L-1} h^2[l]\right\} \times \eta_{LPF}\sigma_N^4[1 + 2DNR] \end{aligned} \tag{66}$$

## ACKNOWLEDGMENTS

The author gratefully thanks Dr. Carlo Bongioanni for the support in the experimental tests. The author also acknowledges the collaboration of many students that have contributed to data simulations and analyses. Among them, I gratefully thank Marco Di Seglio and Michele Stentella.

## REFERENCES

[1] Special Issue on Passive Radar Systems, IEE Proceedings on Radar, Sonar and Navigation, vol. 152, Issue 3, pp. 106–223, June 2005.

[2] Farina A., Kuschel H., "IEEE Aerospace and Electronic Systems Magazine", *Special Issue on Passive Radar Part I & II*, vol. 27, pp. 10-11, 2012.

[3] Lombardo P. and Colone F., "Advanced processing methods for passive bistatic radar," in Melvin, W. L., and Scheer, J. A. (Eds.): 'Principles of Modern Radar: Advanced Radar Techniques', Raleigh, NC: SciTech Publishing, 2012, pp. 739–821.

[4] Griffiths H. and Baker C. J., *An Introduction to Passive Radar*. Artech House, 2017.

[5] Colone F., "Short-range passive radar potentialities" in "Novel Radar Techniques and Applications Volume 1: Real Aperture Array Radar, Imaging Radar, and Passive and Multistatic Radar", Ch. 15, pp. 661-718.

[6] Malanowski M., *Signal Processing for Passive Bistatic Radar,* . Artech House, 2019.

[7] Cherniakov M., Basic principles of forward-scattering radars, in "Bistatic Radar: Principles and Practice", Part III. New York, NY, USA: Wiley, 2007.

[8] Gashinova M., Daniel L., Myakinkov A., Cherniakov M., "Forward scatter radar" in "Novel Radar Techniques and Applications Volume 1: Real Aperture Array Radar, Imaging Radar, and Passive and Multistatic Radar", Chap. 13, pp. 563-619.

[9] Suberviola I., Mayordomo I. and Mendizabal J., "Experimental results of air target detection with a GPS forward-scattering radar", *IEEE Geosci. Remote Sens. Lett.*, vol. 9, no. 1, pp. 47–51,, Jan. 2012.

[10] Kabakchiev C., Garvanov I., Behar V. and Rohling H., "The experimental study of possibility for radar target detection in FSR using L1-based non-cooperative transmitter," *2013 14th International Radar Symposium (IRS)*, Dresden, 2013, pp. 625-630.

[11] Gashinova M., Daniel L., Hoare E., Sizov V., Kabakchiev K., and Cherniakov M., "Signal characterization and processing in the forward scatter mode of bistatic passive coherent location systems", EURASIP J. Adv. Signal Process., vol. 2013, no. 1, pp. 1-13, 2013.

[12] Krysik P., Kulpa K. and Samczyński P., "GSM based passive receiver using forward scatter radar geometry," *2013 14th International Radar Symposium (IRS)*, Dresden, 2013, pp. 637-642.

[13] Kabakchiev C. et al., "Detection parametric imaging and classification of very small marine targets emerged in heavy sea clutter utilizing GPS-Based forward scattering radar", *Proc. 2014 IEEE Int. Conf. Acoust. Speech Signal Process.*, pp. 793-797, 2014.

[14] Contu M., De Luca A., Hristov S., Daniel L., Stove A., Gashinova M., Cherniakov M., Pastina D., Lombardo P., Baruzzi A., and Cristallini D., "Passive multifrequency forward-scatter radar measurements of airborne targets using broadcasting signals," IEEE Transactions on Aerospace and Electronic Systems, vol. 53, no. 3, pp. 1067–1087, June 2017.

[15] Arcangeli A., Bongioanni C., Ustalli N., Pastina D. and Lombardo P., "Passive forward scatter radar based on satellite TV broadcast for air target detection: Preliminary experimental results," 2017 IEEE Radar Conference (RadarConf), Seattle, WA, 2017, pp. 1592-1596.

[16] Colone F., Martelli T. and Lombardo P., "Quasi-Monostatic Versus Near Forward Scatter Geometry in WiFi-Based Passive Radar Sensors," in *IEEE Sensors Journal*, vol. 17, no. 15, pp. 4757-4772, 1 Aug.1, 2017.

[17] Ilioudis C. V. et al., "GNSS Based Passive Radar for UAV Monitoring," 2019 IEEE Radar Conference (RadarConf), Boston, MA, USA, 2019, pp. 1-6.

[18] Clemente C. *et al*., "GNSS based passive bistatic radar for micro-Doppler based classification of helicopters: Experimental validation," *2015 IEEE Radar Conference (RadarCon)*, Arlington, VA, 2015, pp. 1104-1108, doi: 10.1109/RADAR.2015.7131159.

[19] Martelli T., Colone F., Lombardo P., "First Experimental Results for a WiFi-Based Passive Forward Scatter Radar", in IEEE Radar Conference 2016.

[20] Abdullah R. S. A. R., Salah A. A., Aziz N. H. A., and Rasid N. E. A., "Vehicle recognition analysis in lte based forward scattering radar," in 2016 IEEE Radar Conference (RadarConf), May 2016, pp. 1–5.

[21] Losito A., Stentella M., Martelli T. and Colone F., "Automatic vehicles classification approaches for WiFi-based passive forward scatter radar," International Conference on Radar Systems (Radar 2017), Belfast, 2017, pp. 1-6.

[22] Di Seglio M., Colone F., "DVB-T based Forward Scatter Radar for Small Target Surveillance", submitted to IEEE Radar Conference 2020 (Florence, Italy).

[23] Glaser J., "Bistatic rcs of complex objects near forward scatter," IEEE Transactions on Aerospace and Electronic Systems, vol. AES-21, pp. 70–78, 1985.

[24] Willis N., "*Bistatic Radar",* Raleigh, NC, USA, SciTech Publishing, 2005.

[25] Ustalli N., Lombardo P. and Pastina D., "Detection Performance of a Forward Scatter Radar Using a Crystal Video Detector," in IEEE Transactions on Aerospace and Electronic Systems, vol. 54, no. 3, pp. 1093-1114, June 2018.

[26] Hu C., Sizov V., Antoniou M., Gashinova M. and Cherniakov M., "Optimal Signal Processing in Ground-Based Forward Scatter Micro Radars," in IEEE Transactions on Aerospace and Electronic Systems, vol. 48, no. 4, pp. 3006-3026, October 2012.

[27] Searle S., Howard S. and Palmer J., "Remodulation of DVB-T signals for use in passive bistatic radar," in 2010 Conference Record of the Forty Fourth Asilomar Conference on Signals, Systems and Computers, 2010.

[28] ETSI, "Digital Video Broadcasting (DVB)," ETSI, 10 2015. [Online]. Available: http://www.etsi.org/deliver/etsi_en/300700_300799/300744/01.06.02_60/en_300744v010602p.pdf. [Accessed 09 December 2016].

**Fabiola Colone** received the laurea degree (B.S.+M.S.) in Telecommunications Engineering and the Ph.D. degree in Remote Sensing from Sapienza University of Rome, Italy, in 2002 and 2006, respectively. She joined the DIET Dept. (formerly INFOCOM) of Sapienza University of Rome as a Research Associate in January 2006. From December 2006 to June 2007, she was a Visiting Scientist at the Electronic and Electrical Engineering Dept. of the University College London, London, U.K. She is currently an Associate Professor at the Faculty of Information Engineering, Informatics, and Statistics of Sapienza University of Rome.

The majority of Dr. Colone's research activity is devoted to radar systems and signal processing. She has been involved, with scientific responsibility roles, in research projects funded by the European Commission, the European Defence Agency, the Italian Space Agency, the Italian Ministry of Research, and the radar industry. Her research has been reported in over 120 publications in international technical journals, book chapters, and conference proceedings. Dr. Colone has been co-recipient of the 2018 Premium Award for Best Paper in IET Radar, Sonar & Navigation.

Since 2017 she is member of the Board of Governors of the IEEE Aerospace and Electronic System Society (AESS) in which she is currently serving as Vice-President for Member Services, and Editor in Chief for the IEEE AESS QEB Newsletters. She is IEEE Senior Member from 2017 and member of the IEEE AESS Radar System Panel from 2019. Dr. Colone is Associate Editor for the IEEE Transactions on Signal Processing and member of the Editorial Board of the Int. Journal of Electronics and Communications (Elsevier). She served in the technical committee of many international conferences. She was in the organizing committee, as the Student Forum Co-Chair, of the IEEE 2008 Radar Conference (Rome, Italy), and she is currently in the organizing committee, as Special Sessions Co-Chair, of the IEEE 2020 Radar Conference (Florence, Italy). She is also Technical co-Chair of the IEEE Radar Conference 2021 (Atlanta, USA).